



UNIVERSIDAD DE CHILE  
FACULTAD DE CIENCIAS FÍSICAS Y MATEMÁTICAS  
DEPARTAMENTO DE ASTRONOMÍA

SEARCHING FOR RR LYRAE IN DISTANT GALACTIC FIELDS  
USING ULTRAVISTA AND SUDSS

TESIS PARA OPTAR AL GRADO DE  
MAGÍSTER EN CIENCIAS, MENCIÓN ASTRONOMÍA

MARÍA CONSTANZA YOVANINIZ LETELIER

PROFESOR GUÍA:  
RICARDO MUÑOZ VIDAL

MIEMBROS DE LA COMISIÓN:  
SONIA DUFFAU ERAZO  
PAULINA LIRA TEILLERY  
LAURA PÉREZ MUÑOZ

SANTIAGO DE CHILE  
2018

RESUMEN DE LA MEMORIA PARA OPTAR  
AL TÍTULO DE MAGÍSTER EN CIENCIAS, MENCIÓN ASTRONOMÍA  
POR: MARÍA CONSTANZA YOVANINIZ LETELIER  
FECHA: NOVIEMBRE 2018  
PROF. GUÍA: RICARDO MUÑOZ VIDAL

SEARCHING FOR RR LYRAE IN DISTANT GALACTIC FIELDS  
USING ULTRAVISTA AND SUDSS

Búsqueda de RR Lyrae en campos distantes de la Galaxia utilizando UltraVISTA y SUDSS

Buscamos estrellas tipo RR Lyrae en zonas distantes del halo de la Vía Láctea utilizando datos ya existentes: UltraVISTA, una campaña con observaciones en el infrarojo cercano diseñada para obtener imágenes profundas del campo COSMOS, y SUDSS, una extensión del Dark Energy Survey (DES) que añade observaciones en los extremos del tiempo de observación de DES en varios filtros, con la finalidad de observar las curvas de luz de supernovas a alto redshift. Los resultados de la búsqueda de RR Lyrae con estos datos fueron nulos. Ante estos resultados realizamos observaciones simuladas de RR Lyrae, bajo las mismas condiciones de los datos observados, demostrando que la cadencia utilizada en las observaciones no permite la identificación del período de las estrellas RR Lyrae.

Finalmente probamos el método desarrollado con datos de HiTS (High Cadence Transient Survey), una campaña dedicada a detectar transientes en el óptico, principalmente las primeras horas de las explosiones de supernovas. Luego de responder favorablemente a las observaciones simuladas, logramos identificar en los datos de HiTS 2015A un total de 106 RR Lyrae—7 de las cuales se encuentran a una distancia mayor a 100 *kpc*.



# Agradecimientos



Quiero agradecer al profe Ricardo por guiarme en este trabajo y por todo su apoyo mientras intentaba equilibrar mi magíster con mi trabajo como dibujante. A mi comité de tesis, por sus comentarios y consejos que me ayudaron a mejorar mi tesis. A Marta, por su buena onda y su ayuda en todos los protocolos y papeleos existentes. A los funcionarios, por hacer de Calán un lugar mucho más agradable y ameno. A la Tami, por sus riquísimos quequitos de manjar.

Un abrazo para los chicos de la oficina Pequeños Placeres: Jose, Mari, Elise, por los tiempos compartidos, los puzzles y las bajadas a almorzar. A Suaffle, Pola y Bica, por su amistad, su apoyo en tiempos difíciles, y por darme los mejores tiempos que tuve en Calán. Y al resto de mis compañeros del postgrado (Tere, Tetere, Dani, Pia, Patits, Chelo, Richichi, Nina, Gus, Seba, Pepe...), por los buenos almuerzos, las carreras a la van y las experiencias compartidas.

Gracias a mi Pandilla (Aurora, Camilo, Caro, Emilio, Karina, Mireya, Pablo, Pelo, Sotito, Calsito), a Javi y Mini, y a mi familia, por acompañarme desde el principio de todo esto. Y gracias a Rodrigo, por sus ánimos y consejos, por conseguirme un espacio para concentrarme y terminar de escribir esta tesis, y por darme la perspectiva del mundo exterior.



# Contents

<b>List of Figures</b>	<b>vii</b>
<b>1 Introduction</b>	<b>1</b>
1.1 Variable stars . . . . .	1
1.2 On RR Lyrae . . . . .	6
1.2.1 RR Lyrae in Galactic Astronomy . . . . .	9
1.3 This work . . . . .	10
<b>2 Methods</b>	<b>11</b>
2.1 The Lomb-Scargle periodogram . . . . .	11
2.1.1 Window function and aliasing . . . . .	12
2.1.2 Bootstrapping and significance checks . . . . .	13
<b>3 UltraVISTA</b>	<b>15</b>
3.1 Data . . . . .	15
3.2 Photometric calibration and light curve construction . . . . .	17
3.3 Variability criteria . . . . .	19
3.4 Results . . . . .	21
3.4.1 Simulating RRL observations to test UltraVISTA cadence . . . . .	21
<b>4 SUDSS</b>	<b>27</b>
4.1 Data . . . . .	27
4.1.1 Catalogues & Calibration . . . . .	28
4.1.2 Catalog matching and construction of light curves . . . . .	29
4.2 Results . . . . .	32
4.2.1 Simulating RRL observations to test SUDSS cadence . . . . .	33
<b>5 HiTS</b>	<b>36</b>
5.1 Data . . . . .	36
5.1.1 Calibration and light curve construction . . . . .	37
5.2 Results . . . . .	38
<b>6 Discussion</b>	<b>42</b>
<b>Conclusion</b>	<b>43</b>
<b>A HiTS 2015a RRL</b>	<b>45</b>



# List of Figures

1.1	Examples of light curves from different kinds of variable stars . . . . .	2
1.2	The different types of variable stars . . . . .	3
1.3	Location of the Hydrogen and Helium partial ionization zones for stars of different temperatures . . . . .	4
1.4	The instability strip in the Hertzsprung-Russell diagram . . . . .	5
1.5	Direction of sound waves in a star for the fundamental mode and first overtone.	7
1.6	Period-amplitude diagram for RR Lyrae from globular cluster M15. . . . .	7
1.7	Light curves of RRab and RRC stars in the <i>ugriz</i> filters . . . . .	8
2.1	A comparison of a standard periodogram and one with a floating mean model	12
2.2	An example of how the observing window affects the observed signal for a series of regularly-spaced observations . . . . .	13
2.3	An example of how the observing window affects the observed signal for an irregular observing time . . . . .	14
3.1	VIRCAM's pawprint . . . . .	16
3.2	Schematic of the area covered by UltraVISTA on its deep and ultra-deep regions	16
3.3	Histogram of the number of epochs per light curve in each photometric band	18
3.4	Classification of variable objects from the UltraVISTA dataset for 4 different bands . . . . .	20
3.5	Distribution of the periods estimated by the Lomb-Scargle periodogram . . .	22
3.6	Distribution of the periods estimated by the Lomb-Scargle periodogram, separating bright stars from faint stars . . . . .	23
3.7	Some of the periodograms obtained from UltraVISTA data in the J, H and Ks bands . . . . .	24
3.8	The light curves of RR Lyra star DX Del in the H, J and K bands . . . . .	25
3.9	An example of a simulated observation of an RR Lyrae template light curve	25
3.10	A histogram of period distributions from the Catalina Survey and their simulated observations . . . . .	26
4.1	The CCD array used in the Dark Energy Camera . . . . .	28
4.2	Linear fit used for $\sigma$ -clipping calibration . . . . .	29
4.3	All matched catalog objects with over 10 epochs . . . . .	30
4.4	Histogram of the number of epochs per light curve in each photometric band, for the light curves selected after the process described in Sections 4.1.1 and 4.1.2. . . . .	31
4.5	A color-magnitude diagram of all observed stars . . . . .	31



4.6	Distribution of the periods estimated by the Lomb-Scargle periodogram . . .	32
4.7	Examples of Lomb-Scargle periodograms obtained for different SUDSS objects in the $g$ band . . . . .	34
4.8	Histograms of period distributions . . . . .	35
5.1	The fields observed by HiTS in the campaigns 2013A, 2014A and 2015A . . .	37
5.2	A histogram of period distributions from the Catalina survey and their simu- lated observations . . . . .	39
5.3	An example of one the periodograms obtained with HiTS data . . . . .	39
5.4	Period-amplitude diagram for the RRL found with HiTS data . . . . .	40
5.5	Distribution of the found RRL, color coded by heliocentric distance . . . . .	41
5.6	Histogram of the heliocentric distances of the found RRL . . . . .	41
A.1	Phased light curves of RR Lyrae found from HiTS 2015a (1/11) . . . . .	48
A.2	Phased light curves of RR Lyrae found from HiTS 2015a (2/11) . . . . .	49
A.3	Phased light curves of RR Lyrae found from HiTS 2015a (3/11) . . . . .	50
A.4	Phased light curves of RR Lyrae found from HiTS 2015a (4/11) . . . . .	51
A.5	Phased light curves of RR Lyrae found from HiTS 2015a (5/11) . . . . .	52
A.6	Phased light curves of RR Lyrae found from HiTS 2015a (6/11) . . . . .	53
A.7	Phased light curves of RR Lyrae found from HiTS 2015a (7/11) . . . . .	54
A.8	Phased light curves of RR Lyrae found from HiTS 2015a (8/11) . . . . .	55
A.9	Phased light curves of RR Lyrae found from HiTS 2015a (9/11) . . . . .	56
A.10	Phased light curves of RR Lyrae found from HiTS 2015a (10/11) . . . . .	57
A.11	Phased light curves of RR Lyrae found from HiTS 2015a (11/11) . . . . .	58

# Chapter 1

## Introduction

### 1.1 Variable stars

Variable stars are stars whose apparent brightness changes over time. The *General Catalogue of Variable Stars* (GCVS) (Samus et al., 2017) lists more than 100 types and subtypes of these stars. Variable stars are mostly characterized by their *light curves*, a curve that shows the variation of apparent magnitude in time. For better visualization of periodic variables, they are usually shown with their phased light curves, in which the magnitude is shown against phase instead of time. For a variable star of period  $p$ , the phase  $\Phi$  is defined as:

$$\Phi = \frac{t}{P} - \left\lfloor \frac{t}{P} \right\rfloor \quad (1.1)$$

Where  $\Phi$  is the phase,  $t$  the time and  $P$  the period.  $\lfloor t/P \rfloor$  is the floor function of  $t/P$ . Usually two or three phases are shown for visual clarity. Examples of light curves for different types of variable stars are shown in Figure 1.1.

Variable stars can be classified in various types using different criteria. When classified by the mechanism of their variability, variable stars can be separated in two groups: intrinsic variables, which vary in brightness due to an internal physical process, and extrinsic variables, which vary due to external factors, such as being eclipsed by other objects. The subdivisions of these categories are shown in Figure 1.2.

The focus of this thesis is on RR Lyrae stars, a type of pulsating variable star. Pulsating variables are a type of intrinsic variable stars that vary in brightness due to a periodic change in their size, which is caused by the expansion and compression of the outer layers of the star in a process known as the  $\kappa$ -*mechanism* or opacity mechanism (Catelan and Smith, 2014; Carroll and Ostlie, 2017). The opacity  $\kappa$  depends on density and temperature as shown in Kramers' Law (Equation 1.2):

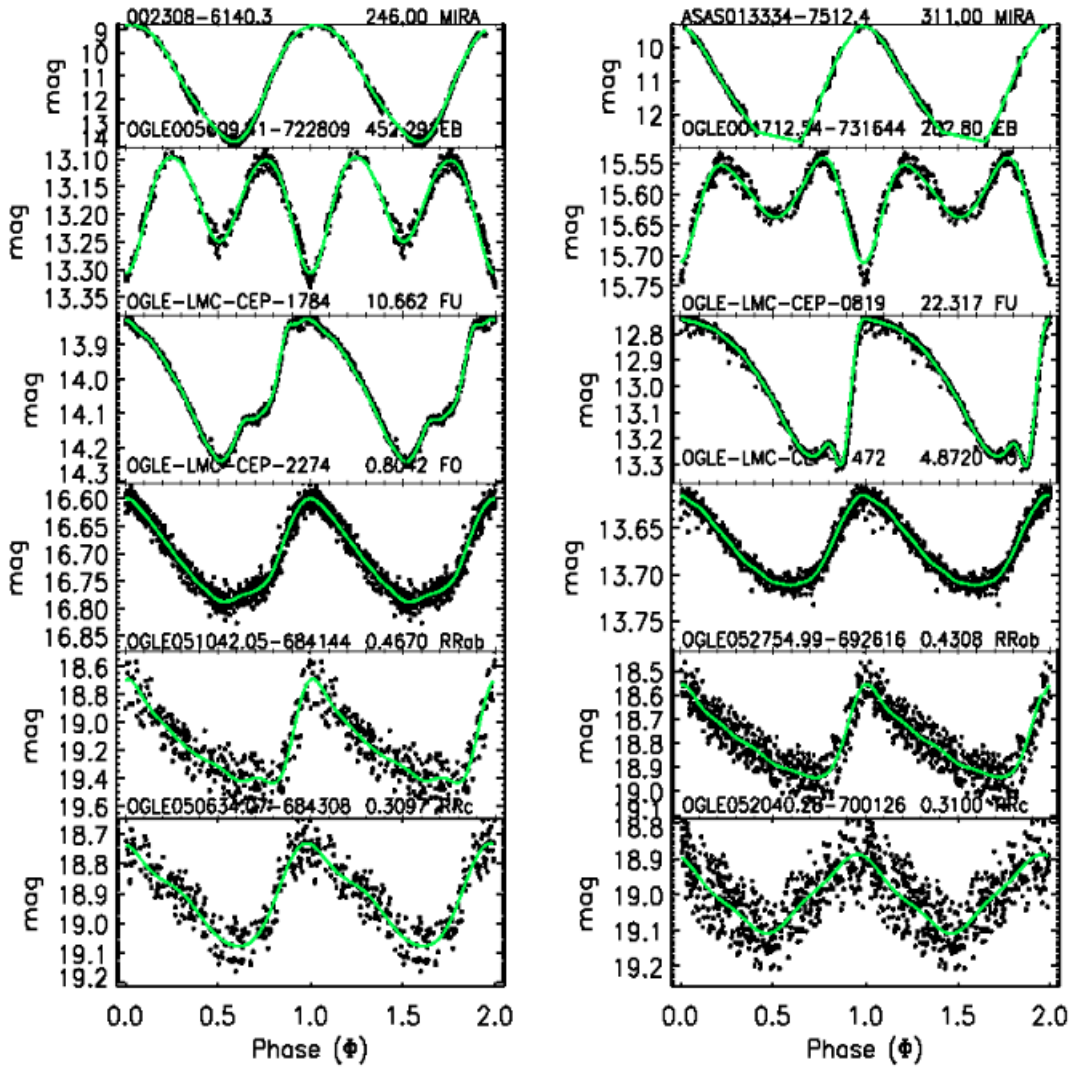


Figure 1.1: Examples of light curves from different kinds of variable stars: Mira variables (MIRA), eclipsing binaries (EB), Cepheid variables (fundamental mode (FU) and first overtone (FO)), and RR Lyrae (RRab and RRC). (Figure from Deb and Singh (2009))

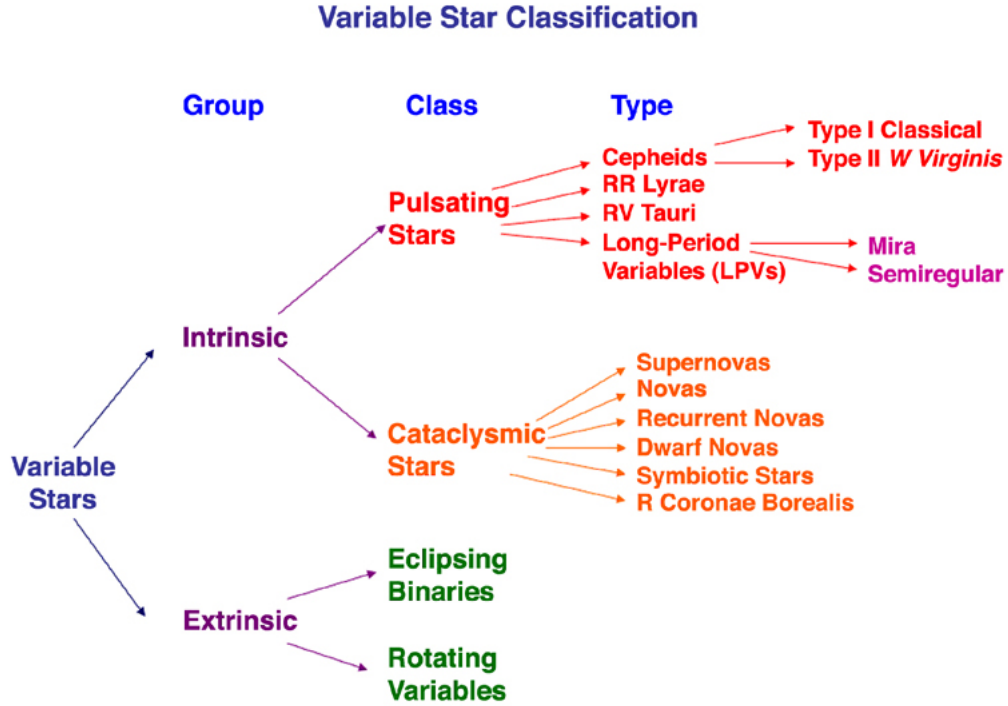


Figure 1.2: The different types of variable stars, classified by the mechanism of their variability.

$$\bar{\kappa} \propto \rho/T^{3.5} \quad (1.2)$$

Where  $\bar{\kappa}$  is the mean opacity,  $\rho$  is the density, and  $T$  the temperature. When the layers of a star are compressed they rise in both density and temperature, but temperature has a higher effect on opacity. Thus, in most cases, opacity decreases with compression. However, in the *partial ionization zones* of a star, part of the energy gained with compression goes towards ionization instead of raising temperature. With a lower increase in temperature compared to the increase in density, the opacity increases. Conversely, as the star expands, ions recombine with electrons and release energy, so the decrease in temperature is lower. Thus, opacity decreases with decreasing density.

This behavior of the opacity law in partial ionization zones, mainly the He II partial ionization zone, makes the layers of the star act like a valve. As the layer compresses, opacity increases and energy flowing to the surface is dammed inside the star, pushing the layers outward. When the star expands, opacity decreases and energy can escape the star. Losing pressure, the layer falls inward due to gravity to begin another pulsating cycle.

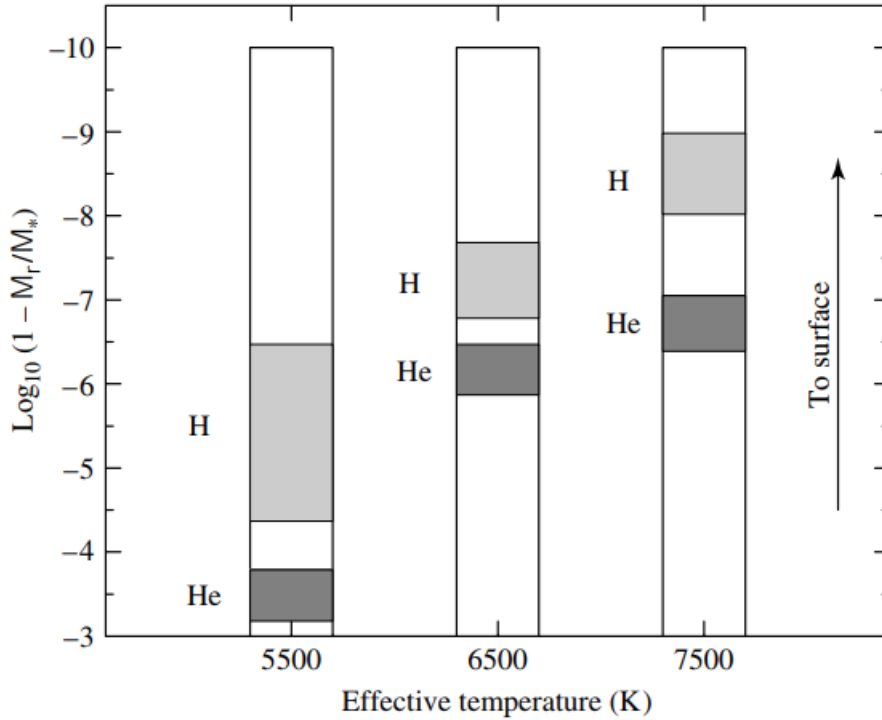


Figure 1.3: Location of the Hydrogen and Helium partial ionization zones for stars of different temperatures. The vertical axis shows the logarithm of the fraction of the star’s mass lying above that point. The bars on the left and right show stars that are either too cold or too hot to drive stellar pulsations. The bar in the middle shows the location of the H and He partial ionization zones in a pulsating star. (Figure from Carroll and Ostlie (2017))

Whether a star pulsates will be determined by the location of the partial ionization zones within the star (Figure 1.3). If the star is too hot, the partial ionization zones will be too close to the surface of the star, and there will not be enough mass to drive stellar pulsations. If the star is colder, the partial ionization zones will be located deeper inside the star. However, energy transport via convection becomes more effective at lower surface temperatures, and in cooler stars this convection dampens the pulsations.

Thus, pulsating stars can be found in a specific range of surface temperatures, where partial ionization zones are located deep enough to drive stellar pulsations, but also have a surface temperature high enough to not have the pulsations damped by convection. This is shown in the Hertzsprung-Russell (H-R) diagram (Figure 1.4) as the *instability strip*. Stars from different stellar populations can be found accross the instability strip, when they intersect in the H-R diagram. Some examples of pulsating star types are Cepheids, W Virginis and RR Lyrae.

An important feature of the instability strip is that it lies at a nearly constant temperature. The luminosity of a star can be estimated using the Stefan-Boltzmann law:

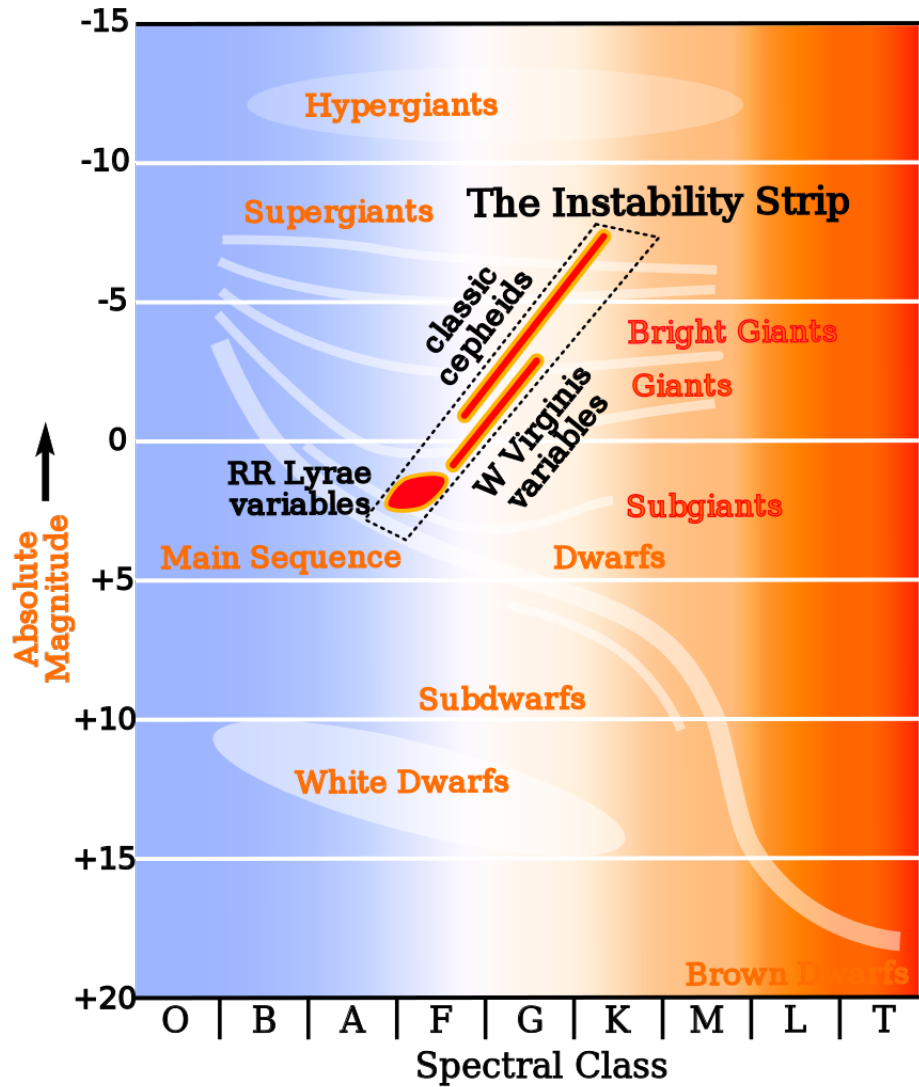


Figure 1.4: The instability strip in the Hertzsprung-Russell diagram. In this area, stars are in a range of temperatures sufficient for the  $\kappa$ -mechanism to take place. The intersection of the instability strip with the different stellar populations leads to the different types of pulsating stars. (Credit: Wikimedia Commons. <https://commons.wikimedia.org/wiki/File:HR-diag-instability-strip.svg>. Accessed: 2018-10-23)

$$L = (4\pi R^2)\sigma T_e^4 \quad (1.3)$$

Where  $L$  is the luminosity,  $R$  is the star's radius,  $\sigma$  is the Stefan-Boltzmann constant, and  $T$  is the star's effective temperature. At nearly constant temperature, the luminosity of a star will mostly depend on its size, and hence, on its density. Additionally, the pulsating period of a star can be estimated by how long it takes a sound wave to cross the diameter of a star of radius  $R$  and constant density  $\rho$ . From this we can define a *period-mean density relation* as:

$$\Pi \approx \sqrt{\frac{3\pi}{2\gamma G\rho}} \quad (1.4)$$

Where  $\Pi$  is the period,  $\gamma$  is the adiabatic index of the star,  $G$  is the gravitational constant, and  $\rho$  is the star's density. From Equations 1.3 and 1.4, and considering a nearly constant temperature, the period-density relationship of the star can be translated into a *period-luminosity relation*. This period-luminosity relation makes pulsating stars important standard candles, as explained in Section 1.2.

## 1.2 On RR Lyrae

RR Lyrae are old, low-mass horizontal branch (HB) stars that fall in the instability strip. They have relatively short periods (between 0.2 and 1.0 days), absolute visual magnitudes of  $\sim +0.6$ , and effective temperatures from 6000 to 7250 K (Catelan and Smith, 2014). RR Lyrae are easily identifiable by the characteristic shape of their light curves and their short periods, which allow to observe them in short time intervals.

The prototype of this star is the star *RR Lyrae*, discovered by Williamina Fleming in 1901 (Pickering et al., 1901), which is also the brightest RR Lyrae star to date. It has a period of 0.56 days and a mean apparent magnitude of  $M_V = 7.195$ .

RR Lyrae are classified by the shape of their light curves into different subclassifications known as Bailey types (Bailey, 1902). RRa and RRb (commonly grouped together as RRab) stars have an asymmetrical sawtooth shaped light curve, an average period of 0.5 days, and a larger amplitude. RRc stars have a more symmetrical (sinusoidal) light curve, an average period of 0.3 days, and smaller amplitudes. This difference in period and amplitude for different Bailey types can be seen in a period-amplitude diagram (also known as a *Bailey diagram*), such as the one in Figure 1.6.

Bailey types are also related to the modes of oscillation of the stars: RRab are known to pulsate in the fundamental mode, while RRc pulsate in the first overtone (Figure 1.5). There

are also RRd stars, which pulsate with in both the fundamental mode and first overtone. An example of representative RRab and RRC light curves in different filters is shown in Figure 1.7.

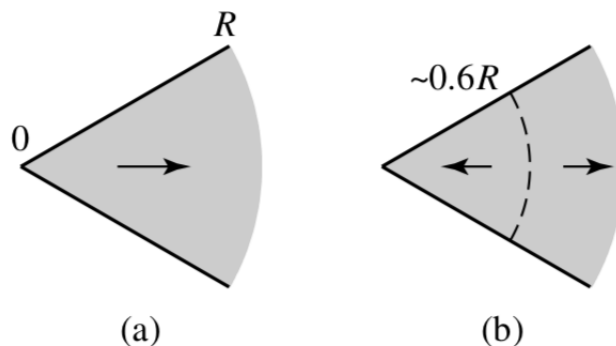


Figure 1.5: Direction of sound waves in a star for the (a) fundamental mode and (b) first overtone. The dashed line represents the nodal line of the sound wave, and the arrows show the motion of the gas particles. (Figure from Carroll and Ostlie (2017))

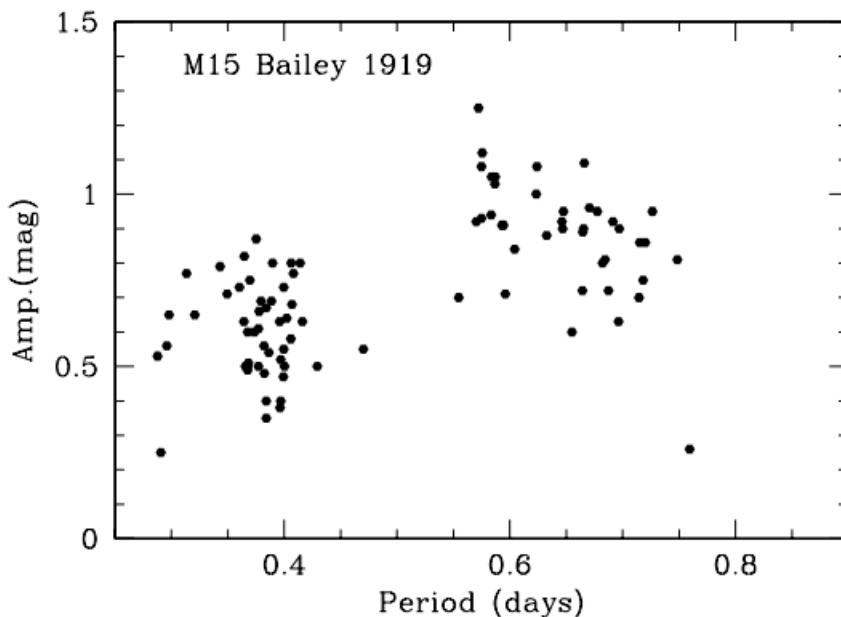


Figure 1.6: Period-amplitude diagram for RR Lyrae from globular cluster M15. The group of stars on the left side are RRC, while the stars on the right side are RRab. (Figure from Smith et al. (2011))

Some RR Lyrae do not have identical light curves over time, showing cycle-to-cycle variations. This is known as the Blazhko effect, first observed by Sergei Blazhko in the RR Lyrae star RW Dra (Blazhko, 1907). This effect is present in nearly 50% of RRab stars (Jurcsik et al., 2009), including RR Lyrae itself (Shapley, 1916). Although this phenomenon has been known for over a century, there is still no agreement to its cause.



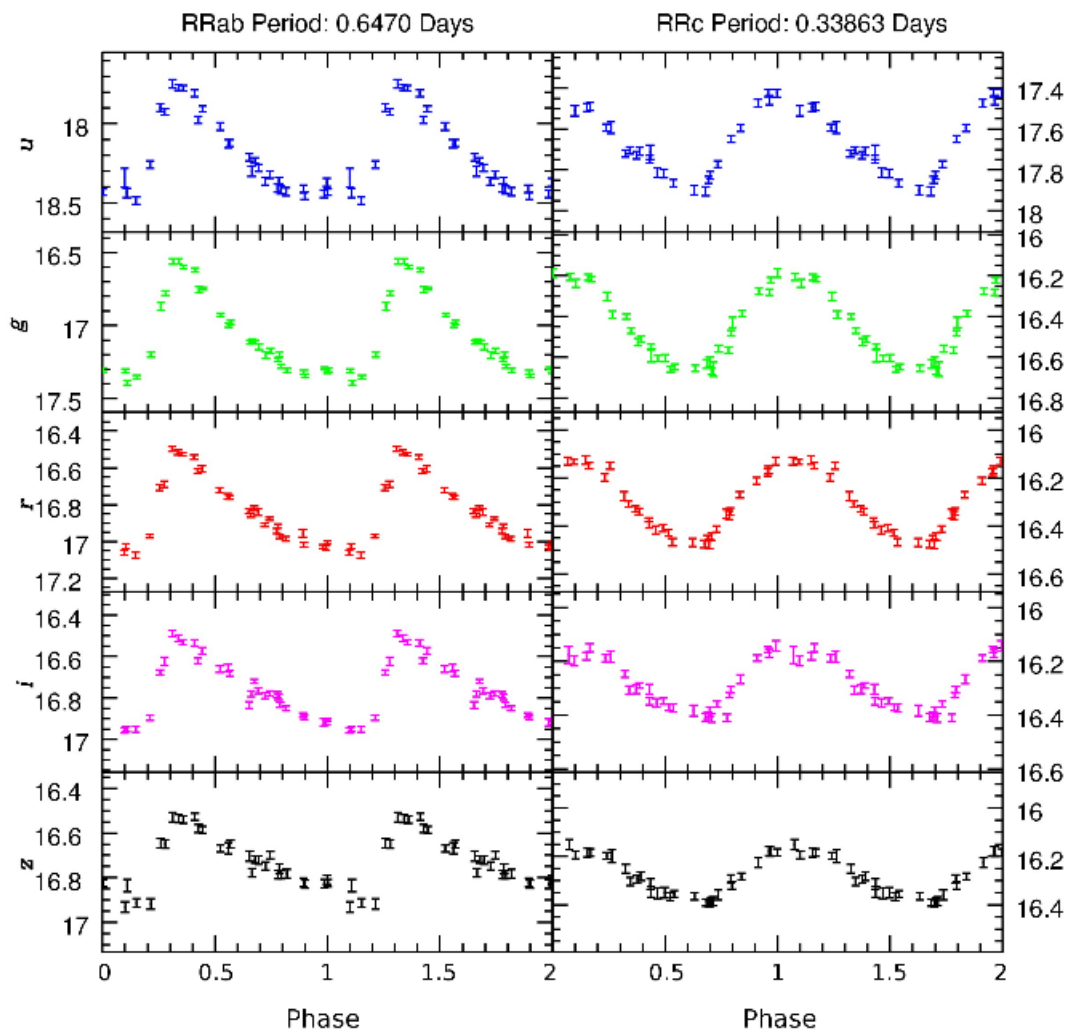


Figure 1.7: Light curves of R Rab and R R c stars in the *ugriz* filters used by the Sloan Digital Sky Survey (Figure from (De Lee, 2008))

One of the main characteristics that make RR Lyrae an interesting object of study is that they are standard candles. Using the star's period-luminosity relationship one can obtain its absolute magnitude  $M$ , and from that calculate the distance  $d$  using the expression in Equation 1.5, where  $\mu$  is known as the *distance modulus*,  $m$  is the apparent magnitude,  $M$  is the absolute magnitude, and  $d$  is the distance to the star in parsecs.

$$\mu = m - M = 5 \log_{10}(d) - 5 \quad (1.5)$$

Period-luminosity relationships, as well as the light curves of RR Lyrae, change for different bands. The amplitude of the light curves increases at smaller wavelengths (as seen in Figure 1.7), reaching up to 4 magnitudes in the ultraviolet range (160nm, Downes et al. (2004)). In the V photometric bandpass the HB is nearly horizontal in the area of the instability strip, so all RR Lyrae in the same stellar population have about the same visual

apparent magnitude. Moving to the infrared there is a well-defined period-luminosity relation (Catelan et al., 2004). Longmore et al. (1986) found a linear relation between the mean K magnitude and the logarithm of the period of the form  $\log P \propto 0.45M_K$ , which is less affected by interstellar reddening and extinction compared to observations in the optical range.

Finding zero points to calibrate the expressions for period-luminosity or period-luminosity-metallicity relations for RR Lyrae is a challenging task, as even the closest stars of this type are too distant for accurate parallax measurements from ground-based observations. Benedict et al. (2011) determined parallaxes for near RR Lyrae stars using the Hubble Space Telescope (HST), with which they obtained calibrations for  $K$ - $\log P$  and  $M_V$ - $[Fe/H]$  relations. More accurate calibrations are currently being done with the astrometry done by Gaia, such as Muraveva et al. (2018).

### 1.2.1 RR Lyrae in Galactic Astronomy

The Milky Way is the most studied galaxy in the Universe and it provides astronomers with insight on the physical processes of galaxies in a broader context. Its halo is a region of particular interest, as its current observable properties such as the distribution of stars can be used to reconstruct the Galaxy’s merger history (Johnston et al., 2008).

The  $\Lambda$  Cold Dark Matter model ( $\Lambda$ CDM, with  $\Lambda$  being the cosmological constant) is currently the most accepted cosmological model, as it explains properties like the cosmic microwave background, the large-scale structure in the distribution of galaxies, the abundances of hydrogen and helium, and the accelerating expansion of the Universe. However, this model shows discrepancies at smaller scales, such as the one between the number of dark matter subhalos predicted by simulations of the  $\Lambda$ CDM model and the number of satellite galaxies known to exist in the Local Group. This is usually referred to as the *missing satellites problem*. The most popular interpretation of this problem is that dark matter halos that are too small will not form stars, but recent discoveries of ultra-faint dwarf satellites point out at the possibility that there might be many dwarf galaxies that are too faint to have been detected with current observations.

Whatever the solution to this problem is, current models for the Milky Way’s structure, dynamical properties, and formation history depend heavily on its total mass and mass profile. However, the total mass of the Galaxy is currently known only within a factor of two (Eadie and Harris, 2016; Ablimit and Zhao, 2017). Most of the Galaxy, especially its outer region, is comprised of dark matter, which is not possible to observe directly. The most reliable way to estimate the amount of dark matter in the Galaxy is by observing the effect it has on baryonic mass, such as the outer rotation curve of the Galaxy, and the kinematics of distant tracer objects such as globular clusters, dwarf galaxies, stellar streams, and halo stars.

In this context, RR Lyrae—old, Population II, low-mass stars—are key tracers for both globular clusters and dwarf galaxies in the Milky Way halo, as they are easily identifiable, have short periods, and give reliable distances. Over 80% of all variables known in globular clusters are RR Lyrae (Clement et al., 2001), and at least one RR Lyrae has been found in every Milky Way dwarf galaxy that has been searched for them (Vivas et al., 2016)—including the least luminous Milky Way satellite, Segue 1 (Simon et al., 2011). At the same time, distances to RRL can be estimated with a precision of  $\sim 6\%$  with optical data (Sesar et al., 2013). Therefore, RR Lyrae can trace faint Milky Way satellites that would otherwise be very difficult to find with other methods, making them an invaluable tool for Galactic astronomy. In the same vein, RR Lyrae stars represent the best opportunity to identify distant mass tracers in the outer halo.

### 1.3 This work

Searching for distant RR Lyrae in the Galactic halo is of great use to the study of the Milky Way, as explained in Section 1.2.1. There are currently no deep, large area surveys looking for tracers such as RRL in the outer regions of the Galactic halo ( $> 100kpc$ ), but there are other surveys which also work with time series in these fields, whose existing data can be used to search for RRL as well.

In this thesis I use data from three existing surveys in the infrared and optical: UltraVISTA, SUDSS, and HiTS, to search for RR Lyrae in distant galactic fields using the generalized Lomb-Scargle periodogram. Although these surveys are not originally designed to search for RRL, they have characteristics, such as photometric depth and location, that make these datasets worth studying. However, in two of these surveys the results are null, which leads to an analysis of the impact that cadence has on searching for periodic variables like RR Lyrae.

Chapter 2 describes the methods used in this work: the generalized Lomb-Scargle periodogram and the use of bootstrapping for significance checks. Chapter 3 describes the data from the UltraVISTA survey, analysis and results. Chapter 4 covers the work done with data from the Search Using DEcam for Superluminous Supernovae (SUDSS). Chapter 5 describes the data from the High Cadence Transit Survey (HiTS) on its 2015A campaign. In Chapter 6 the obtained results are discussed.

# Chapter 2

## Methods

### 2.1 The Lomb-Scargle periodogram

Many techniques have been developed for determining periodic signals in astronomical time series. They generally include running a series of trial periods and measuring the goodness of fit of each, to find the model that best estimates the observed signal. Some of these methods include the use of the Fourier transform and power spectra, least squares methods, and the use of Bayesian probability.

For this work I am using a version of the Lomb-Scargle periodogram, a method which is mostly Fourier-based but can also be seen as a least squares method, and derived from a Bayesian approach (VanderPlas, 2017). The classical Lomb-Scargle periodogram, as defined in Lomb (1976), is shown in equations 2.1 and 2.2.

$$p(\omega) = \frac{1}{\sum_i y_i^2} \left( \frac{[\sum_i y_i \cos\omega(t_i - \tau)]^2}{\sum_i \cos^2\omega(t_i - \tau)} + \frac{[\sum_i y_i \sin\omega(t_i - \tau)]^2}{\sum_i \sin^2\omega(t_i - \tau)} \right) \quad (2.1)$$

Where  $\tau$  is a normalization parameter such that  $\sum_i \cos\omega t_i \sin\omega t_i = 0$ . It is obtained as:

$$\tan 2\omega\tau = \frac{\sum_i \sin 2\omega t_i}{\sum_i \cos 2\omega t_i} \quad (2.2)$$

This method is equivalent to fitting a sine function of the form  $y = a\cos(\omega t) + b\sin(\omega t)$  to a set of points  $(t_i, y_i)$ , where  $\omega = 2\pi/p$  is the trial frequency for a trial period  $p$  (in days). From here we obtain an estimate Fourier power for each frequency of oscillation—a way to measure the goodness of fit of a sinusoid with said trial frequency to the measured data. This will show as peaks in the periodogram, with better fits having the highest peaks. However, there are some shortcomings with the original Lomb-Scargle periodogram. This method doesn't account for measurement errors, and it assumes that the mean of the observed data is the same as the mean of the fitted sine function - which is a poor estimation in cases where the

faintest points of the lightcurve cannot be observed, as is the case in the example of Figure 2.1.

For this work I am using the *generalized* Lomb-Scargle periodogram as described in Zechmeister and Kürster (2009), implemented in the AstroML module for Python (Vanderplas et al., 2012). This periodogram accounts for irregular time intervals and measurement errors, works with a floating mean, and is less susceptible to aliasing (see Section 2.1.1).

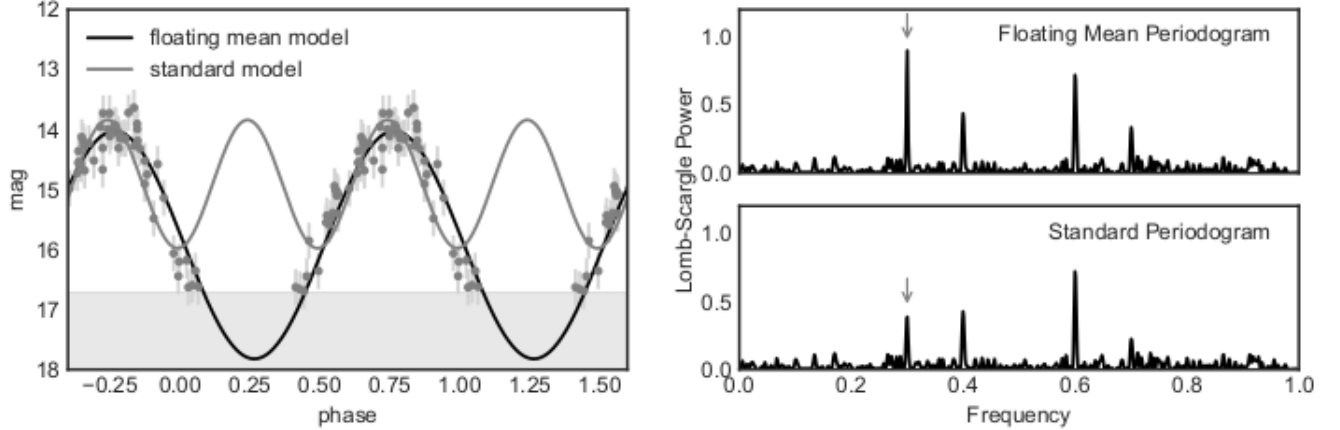


Figure 2.1: A comparison of a standard periodogram and one with a floating mean model. The left panel shows the data points taken for a star in which magnitudes higher than  $\sim 17$  are not observed (denoted by the grey area). The standard Lomb-Scargle periodogram, shown in the lower right panel, fails to detect the original period, as seen by the grey line in the left panel. The floating mean periodogram, shown in the upper right panel, accomplishes to recover the original period and gives a more accurate fit, as shown by the black line in the left-side panel. (Figure from VanderPlas (2017))

### 2.1.1 Window function and aliasing

Since the Lomb-Scargle periodogram is motivated by a Fourier approach, one must consider the effect the observing window will have on trying to find the true period.

The observed signal  $g_{obs}(t)$  can be described as a pointwise product between the real signal,  $g(t)$ , and a window function  $W(t)$ , which is a step function that equals 1 at the times of observation and 0 elsewhere. Taking this to the Fourier plane, the Fourier transform of the observed signal will be the convolution of the real signal transform and the window transform:

$$g_{obs}(t) = g(t)W(t) \quad (2.3)$$

$$\mathcal{F}(g_{obs}) = \mathcal{F}(g) * \mathcal{F}(W) \quad (2.4)$$

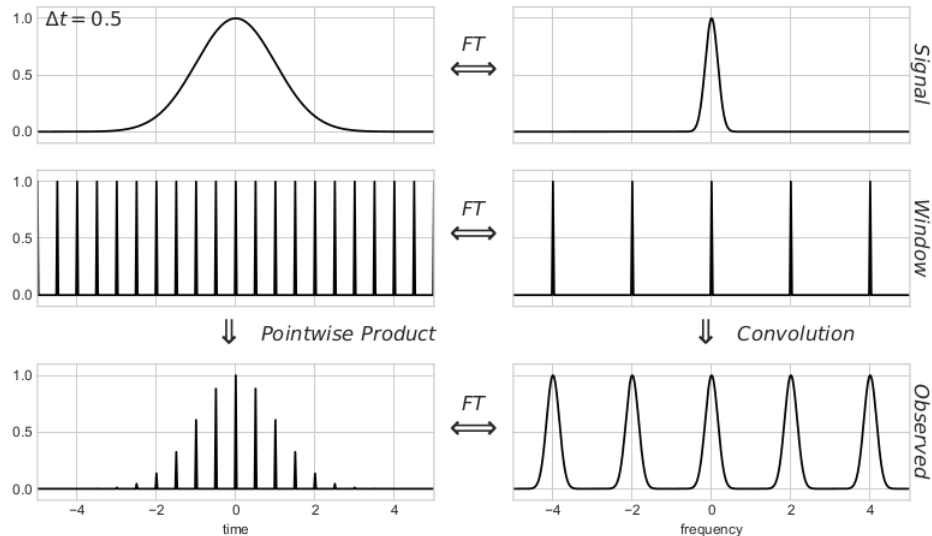


Figure 2.2: An example of how the observing window affects the observed signal and its respective Fourier transform, for a series of regularly-spaced observations. The left side shows the original signal, the window function, and the pointwise product of the two, which is the observed signal. The panels on the right side show the Fourier transform of panels on the left side. (Figure from VanderPlas (2017))

An example of this is shown in Figure 2.2. For an observation done in regular intervals, it is clear to see how the convolution between the Fourier transform of the signal and the window function creates a series of aliases of the signal transform, with a spacing of  $1/T$ . However, when a time series has irregular sampling, the window function’s transform is no longer regular, and aliases make the real signal harder or impossible to detect. An example of this is shown in Figure 2.3.

## 2.1.2 Bootstrapping and significance checks

In order to verify that the results obtained by the Lomb-Scargle periodogram are *significant* enough (that is, that the probability that they have been obtained by chance is low), I run a bootstrap analysis of the results yielded by Lomb-Scargle using `lomb_scargle_bootstrap`, also available from the AstroML module.

Bootstrapping is a statistical method that falls under the class of *resampling* methods. It works by doing resampling with replacement from a known sample, to infer about an unknown population. From this we can estimate a level of significance, which can be used to reject the null hypothesis (that there’s no periodic signal and any detection is only due to noise or sampling conditions). In this case, the bootstrap analysis determines the likelihood of a certain power level being exceeded just by chance.

All periodograms in this work are shown with cuts for 10% and 5% significance, which

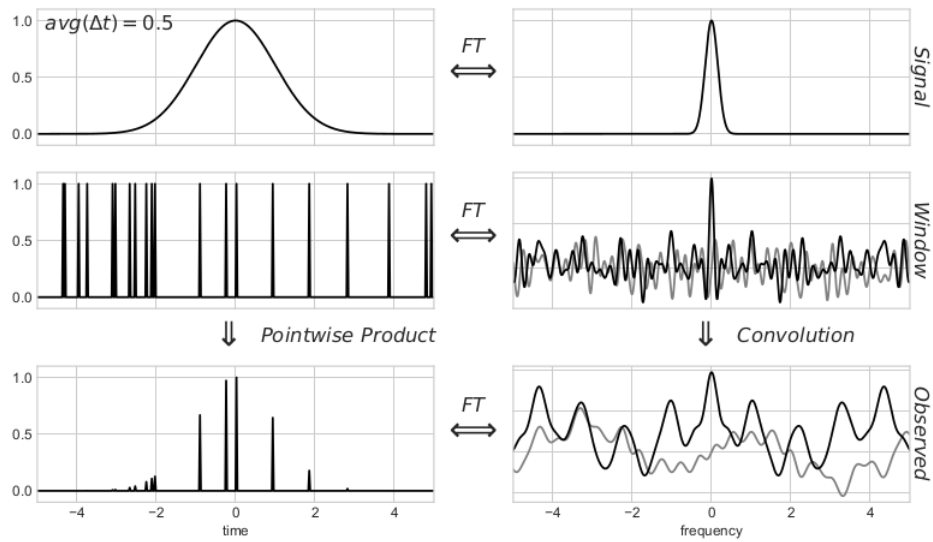


Figure 2.3: Another example of how the observing window affects the observed signal, now for an irregular observing time. The irregular observing window makes the window transform more noisy, which difficulties finding the true signal in the observed convolution. (Figure from VanderPlas (2017))

means that the peaks that cross these thresholds only have a 10% or 5% probability to be a result of noise or sampling conditions alone.

# Chapter 3

## UltraVISTA

### 3.1 Data

The UltraVISTA survey (McCracken et al., 2012) is an Ultra Deep near infrared (NIR) survey of the COSMOS field, covering an area of  $1.5\text{deg}^2$ . It is done using the instrument VIRCAM (Dalton et al., 2006) in the VISTA Survey Telescope of the European Southern Observatory (ESO) (Sutherland et al., 2015). VIRCAM works with 16 independent infrared detectors (Figure 3.1). The data used were taken from December 2009 to April 2014, in which UltraVISTA imaged all of the COSMOS field repeatedly in 5 different bands (YJHKs and NB118). The pixel scale of the images is 0.34 arcsec/pixel. The data reduction pipeline is done by the Cambridge Astronomy Survey Unit (CASU) (CAS). This process includes dark subtraction, flat-fielding, sky-subtraction, astrometric and photometric calibration.

UltraVISTA is a survey focused on obtaining deep and ultra deep images of the COSMOS field (Figure 3.2), and the final product of this survey are stacked images along with their corresponding weight maps in each band. We will work with the individual Observation Blocks in each band, which are images corresponding to 0.5 or 1 hour of exposure. They were produced by CASU and provided by the survey team for the light curve construction in Sánchez et al. (2017)

The average  $5\sigma$  magnitude limit for each band is 23.3, 23.1, 22.2, and 22.1 for the Y, J, H and Ks bands respectively. The average error of the images is 0.15 *mag* in the Y band, 0.15 *mag* in J, 0.17 *mag* in H and 0.16 *mag* in Ks. This survey covers a small section of the sky, but it reaches high magnitudes, which makes it interesting to search for distant RR Lyrae. This survey only covers  $1.5\text{deg}^2$  and, based on results from previous surveys (Zinn et al., 2014; Drake et al., 2013b), we can estimate to find around 3 RR Lyrae in this area. However, considering the magnitude limits of the survey, it could find RRab stars up to 260 kpc away.



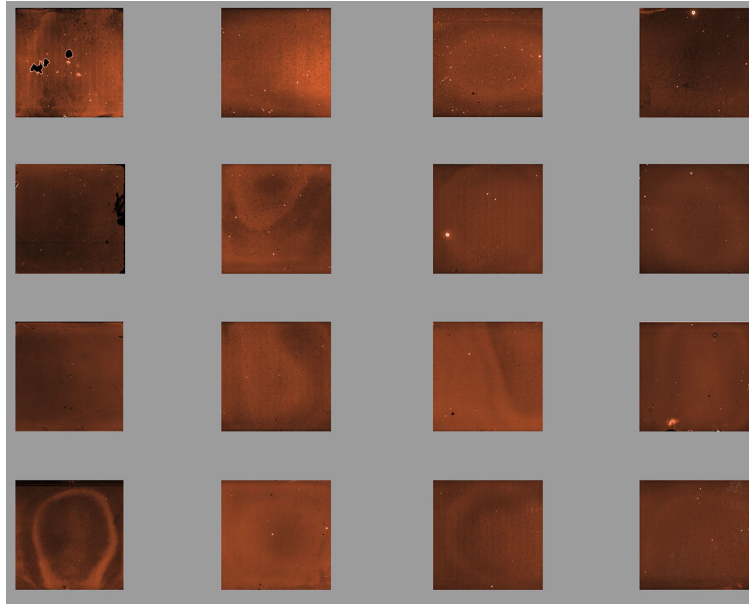


Figure 3.1: VIRCAM’s pawprint. VIRCAM has 16 separate infrared detectors, which are placed separate from each other due to technical constraints. (credit: ESO. [https://www.eso.org/public/images/vcam\\_cc/](https://www.eso.org/public/images/vcam_cc/). Accessed: 2018-10-23)

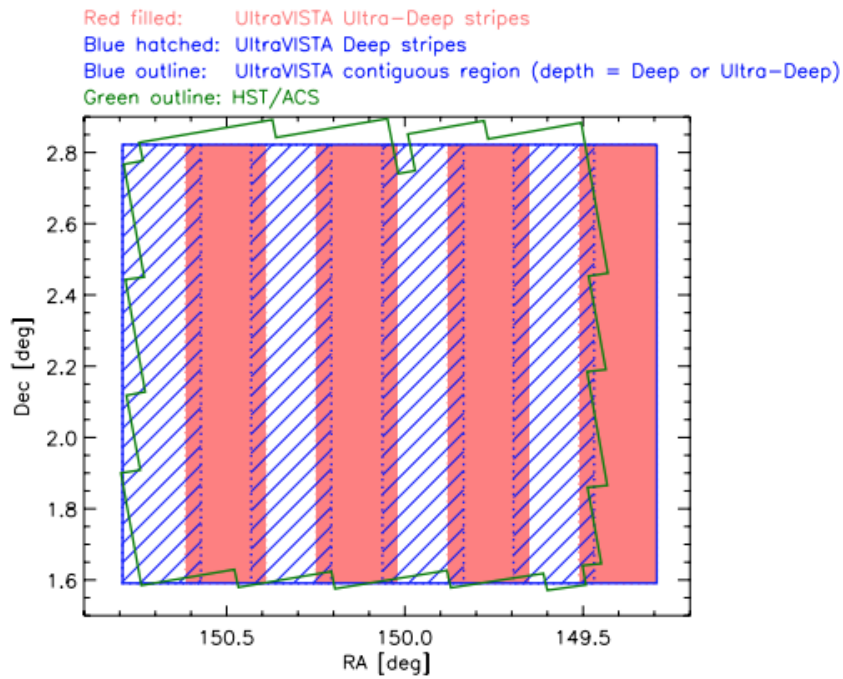


Figure 3.2: Schematic of the area covered by UltraVISTA on its deep and ultra-deep regions (Figure from McCracken et al. (2012))

## 3.2 Photometric calibration and light curve construction

In this section I describe the calibration and construction of light curves from UltraVISTA data, carried out in their entirety by Sánchez et al. (2017). UltraVISTA images consist of 16 separate images, one per detector (Figure 3.1). Detector 16 was not considered, as it was known to have an unstable gain. After the initial photometric calibration done by CASU, a PSF homogenization was performed on the images to avoid false variability detections by differences in seeing. Images with a seeing worse than 1.0" were discarded.

The catalogs were generated with the public package SExtractor (Bertin and Arnouts, 1996), a photometry software that generates catalogs from FITS formatted images. It takes a set of input parameters from the user (such as background estimation parameters, weight images, detection thresholds, and others), and exports a catalog with a filetype (FITS, VOTable, ASCII) and outputs (flux, magnitude, errors, pixel or world coordinates, among others) determined by the user. After the catalogs were generated, photometric errors were calculated with a method similar to the one implemented by Gawiser et al. (2006), to ensure there is no false variability due to these errors.

A Ks-selected catalog of the COSMOS/UltraVISTA field by Muzzin et al. (2013) was used to check the quality of UltraVISTA photometry, particularly the *contamination parameter*, which indicates when an object's photometry has been contaminated by a nearby bright star. Only those sources with a contamination parameter equal to zero were saved for this work.

To produce the calibrated catalogs, the catalogs generated by SExtractor were cross-matched with the UltraVISTA Data Release 3 (DR3) catalog in each band. The sources selected to generate light curves are those that SExtractor had classified as stars (`CLASS_STAR`  $\geq 0.9$ ) with good photometry (`FLAGS` = 0). Then an additional photometric calibration was done using a linear fit similar to Cartier et al. (2015) (detailed in Section 4.1.1), to account for possible non-linearities in the detectors.

Finally, the calibrated catalogs were cross-matched to generate preliminary light curves. A  $\sigma$ -clipping process was applied to clean these preliminary light curves from outliers that might give false variability detections, and those with three epochs or more left after the  $\sigma$ -clipping were saved as final light curves.

The UltraVISTA project did not observe the same number of epochs in every photometric band. On average the Y band has 39 epochs, the J band has 40, the H band has 64 and the Ks band has an average of 75. Figure 3.3 shows the distribution in the number of epochs per light curve for each photometric band. The light curves used in this work were calibrated by Sánchez et al. (2017), and are used with their permission.

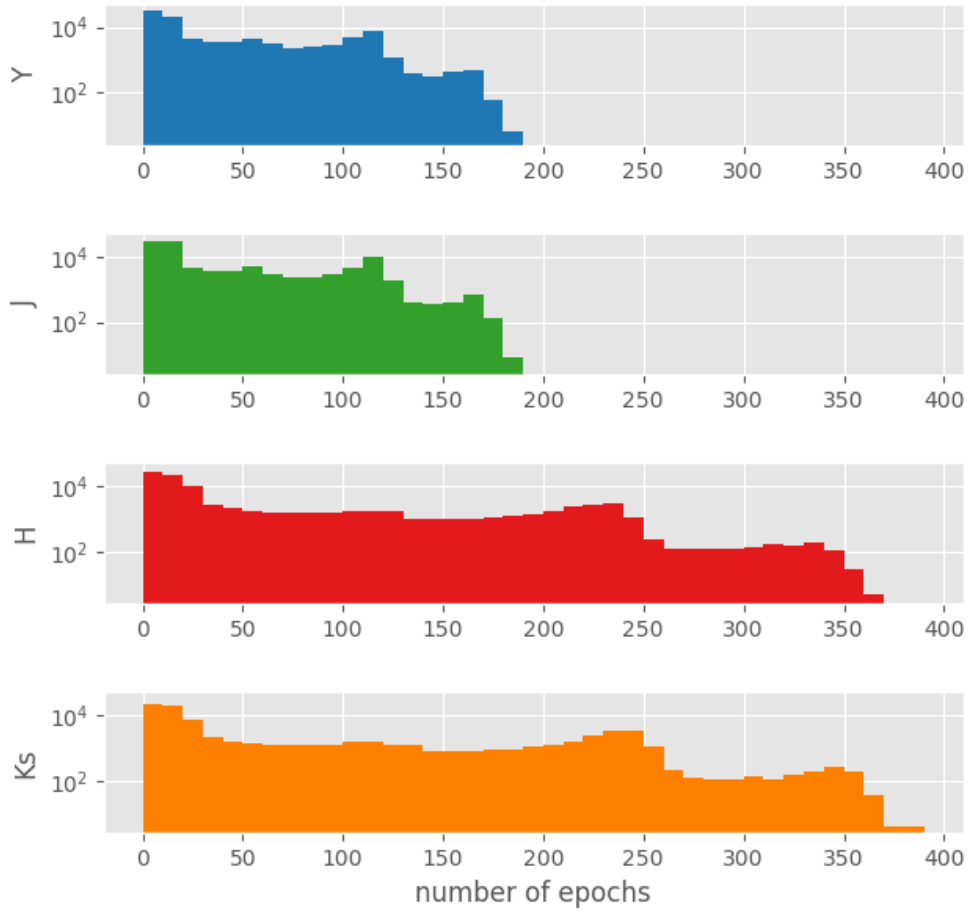


Figure 3.3: Histogram of the number of epochs per light curve in each photometric band.

### 3.3 Variability criteria

In order to find possible candidates for RR Lyrae, I separated those objects from the Ultra-VISTA sample that could be classified as variable. To do this I used the  $P_{var}$  and excess variance  $\sigma_{rms}^2$  parameters.

$P_{var}$  (McLaughlin et al., 1996) is related to the probability of a source being variable. It is defined from the  $\chi^2$  value of the light curve as:

$$\chi^2 = \sum_{i=1}^{N_{obs}} \frac{(x_i - \bar{x})^2}{\sigma_{err,i}^2} \quad (3.1)$$

Where  $x_i$  is the magnitude at each epoch,  $\sigma_{err,i}$  is its error,  $\bar{x}$  is the mean magnitude and  $N_{obs}$  is the number of epochs of the observed object.  $P_{var} = P(\chi^2)$ , and it measures the probability that a  $\chi^2$  lower or equal to the one observed could occur by chance for a nonvariable object. Therefore,  $P_{var}$  shows the probability of the object being intrinsically variable.

The excess variance  $\sigma_{rms}^2$  (Nandra et al., 1997; Allevato et al., 2013; Cartier et al., 2015) measures the probability amplitude. It is defined as:

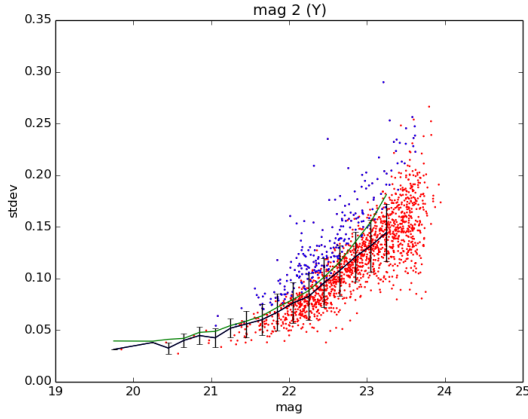
$$\sigma_{rms}^2 = \frac{1}{N_{obs} \bar{x}^2} \sum_{i=1}^{N_{obs}} [(x_i - \bar{x})^2 - \sigma_{err,i}^2] \quad (3.2)$$

$$err(\sigma_{rms}^2) = \frac{S_D}{\bar{x}^2 N_{obs}^{1/2}} \quad (3.3)$$

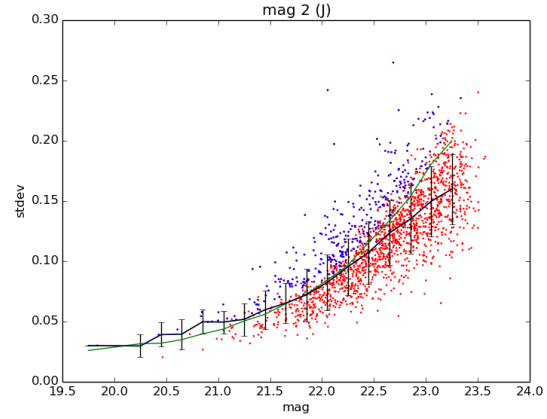
$$S_D^2 = \frac{1}{N_{obs}} \sum_{i=1}^{N_{obs}} N_{obs} [(x_i - \bar{x})^2 - \sigma_{err,i}^2] - \sigma_{rms}^2 \bar{x}^2 \quad (3.4)$$

When the intrinsic amplitude of the variability, corrected by photometric errors, ( $\sigma_{rms}^2 - err(\sigma_{rms}^2)$ ) is larger than zero, the object is classified as variable.

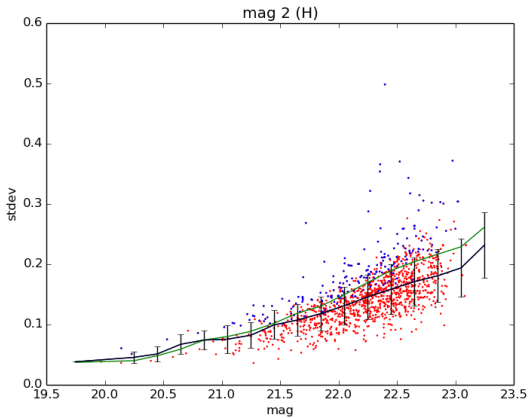
Following the procedure done in Sánchez et al. (2017), an object will be classified as intrinsically variable if  $P_{var} \geq 0.95$  and  $(\sigma_{rms}^2 - err(\sigma_{rms}^2)) > 0$ . This classification is shown for each band in Figure 3.4, where the points marked in blue have been classified as variable and the ones in red as nonvariable.



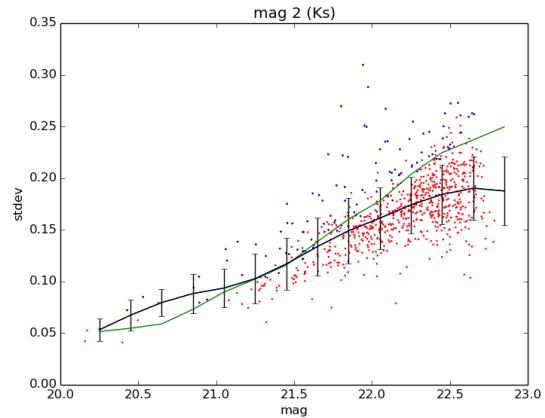
(a) Y band



(b) J band



(c) H band



(d) Ks band

Figure 3.4: Classification of variable objects from the UltraVISTA dataset for the Y, J, H, and Ks bands. The horizontal axis shows the mean magnitude of each object, while the vertical axis shows the standard deviation of the object’s magnitude. The line in black shows the median of the standard deviation of the objects’ magnitudes for each magnitude bin, while the line in green shows the median of the error of the objects’ magnitudes. Objects in blue are considered as variable according to the method explained in Section 3.3.

## 3.4 Results

To search for RR Lyrae on this dataset, I developed a code using the Lomb-Scargle periodogram as described in Section 2.1. After being tested with successful results recovering the periods from Medina et al. (2018), I ran the same process with the light curves from UltraVISTA.

Figure 3.5 shows the distributions of the estimated periods obtained in each band. They show a clear peak in very specific periods, which is a result of aliasing (see Section 2.1.1). This aliasing is more prominent in the brighter end of the sample, as seen in Figure 3.6.

Unfortunately, no RR Lyrae were detected when running the periodograms to search for periodicity. Some of the periodograms obtained, with their respective folded light curves, are shown in Figure 3.7. These periodograms show clear peaks and a consistent periodic pattern, but none of the folded light curves resemble those of an RR Lyrae in their respective filters. If an RRL population was to be found, it is expected from the literature that most of them will be RRab (Smith, 2004). However, the only light curves that could resemble those of a variable star were more symmetrical, closer to the light curve of an RRc, but since it does not match the expected distribution they were not considered.

### 3.4.1 Simulating RRL observations to test UltraVISTA cadence

In light of the null results obtained when analyzing UltraVISTA data, I test whether the cadence of the data we have is suitable for detecting RR Lyrae. For this I ran a series of simulated observations of RR Lyrae and their following analyses using the Lomb-Scargle periodogram.

For these simulated observations I use a template of an RRab Lyrae light curve - DX Del, as observed in the H, J, and K bands (Skillen et al., 1989), chosen as a random example from the templates available at the VVV Templates Project (Angeloni et al., 2014) (Figure 3.8). This template, which is in phase, will be used to generate artificial RRL light curves with different periods, with periods sampled at random from a period distribution of known RR Lyrae taken from the Catalina Survey (Drake et al., 2013b).

With this I simulate an observation of the generated light curves by using the same cadence as one of the real UltraVISTA observations, which is also chosen at random. This simulated sampling is then put through the Lomb-Scargle periodogram, to test if the original period can be recovered.

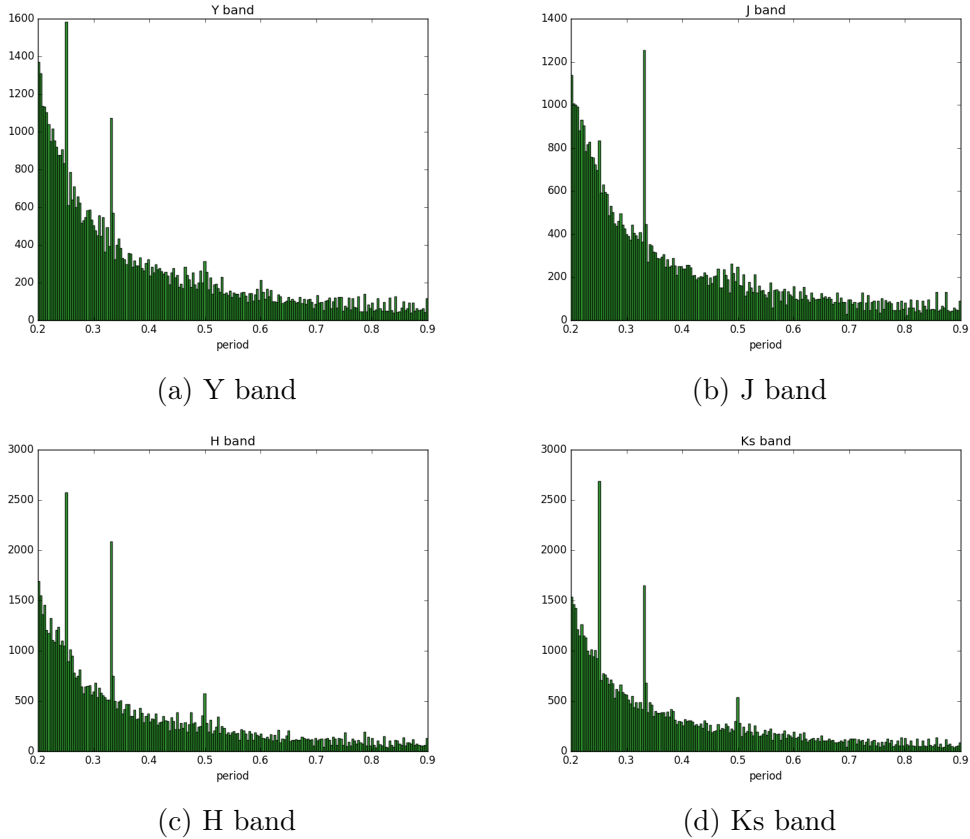


Figure 3.5: Distribution of the periods estimated by the Lomb-Scargle periodogram. The specific peaks that deviate from the general distributions are a result of aliasing.

Figure 3.9 shows an example of the aforementioned simulations where the period is recovered. On the top left is the RR Lyrae light curve template I am using, to which a period taken at random from the Catalina Survey RR Lyrae period distribution will be assigned. On the top right corner is the simulated data sampling - the blue line shows the magnitude of the observed RR Lyrae changing with time, while the red dots indicate the data collected by the simulated sampling - which in this case uses the same cadence as one of our UltraVISTA light curves, chosen at random. A fixed error of 0.05 magnitudes is given to each observed magnitude.

The bottom right corner of the figure shows the Lomb-Scargle periodogram of the simulated data sampling, with the dotted lines representing the 10% and 5% significance levels obtained from a bootstrap analysis (see Section 2.1.2). On the bottom left is the recovered folded light curve, using the best period estimated from the Lomb-Scargle periodogram and the observed magnitudes.

After estimating a period of all simulated observations using the Lomb-Scargle periodogram, I compare the final period distribution with the original one from the Catalina Survey. In Figure 3.10 is the period distribution of 500 RR Lyrae sampled at random from the Catalina Survey (in blue). This distribution peaks around 0.6 days, the average period

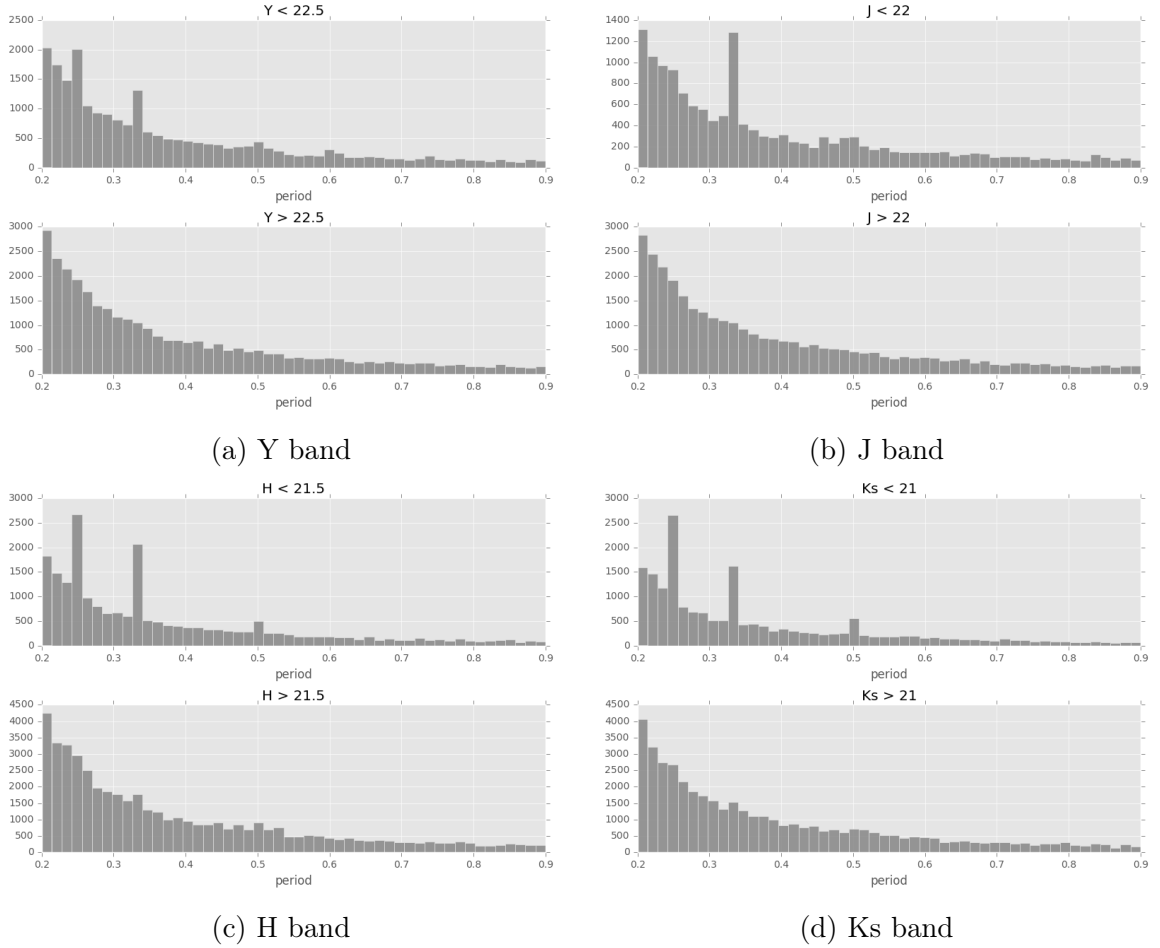


Figure 3.6: Distribution of the periods estimated by the Lomb-Scargle periodogram, separating bright stars from faint stars.

for RRab types, the most common type or RR Lyrae.

On the left side of Figure 3.10, the distributions in red show the periods obtained by the simulated observations of these stars, using the cadence from 500 UltraVISTA light curves chosen at random. This distribution shows two different peaks, with the highest one being between 0.2 and 0.3 days. This matches the aliasing that is shown in Figure 3.5.

On the right side of Figure 3.10, the distributions in red are only the periods obtained in the simulations that recovered the original RRL period. Here we consider a period as recovered when the period with the highest peak and the original period have a difference of  $|p_{best} - p_{original}| < 0.01$  days. The fraction of periods recovered was 32.4% in the J band, 34.4% in the H band, and 39.8% in the Ks band. Although no RRL were found in the actual sample, this recovery rate shows that they could have been found if the survey covered a larger area in the sky. Another point to consider is the exposure of the images from UltraVISTA, which goes from 0.5 to 1 hour of exposure. Having a high exposure might hinder a search for variables with short periods (from 7 to 14 hours).



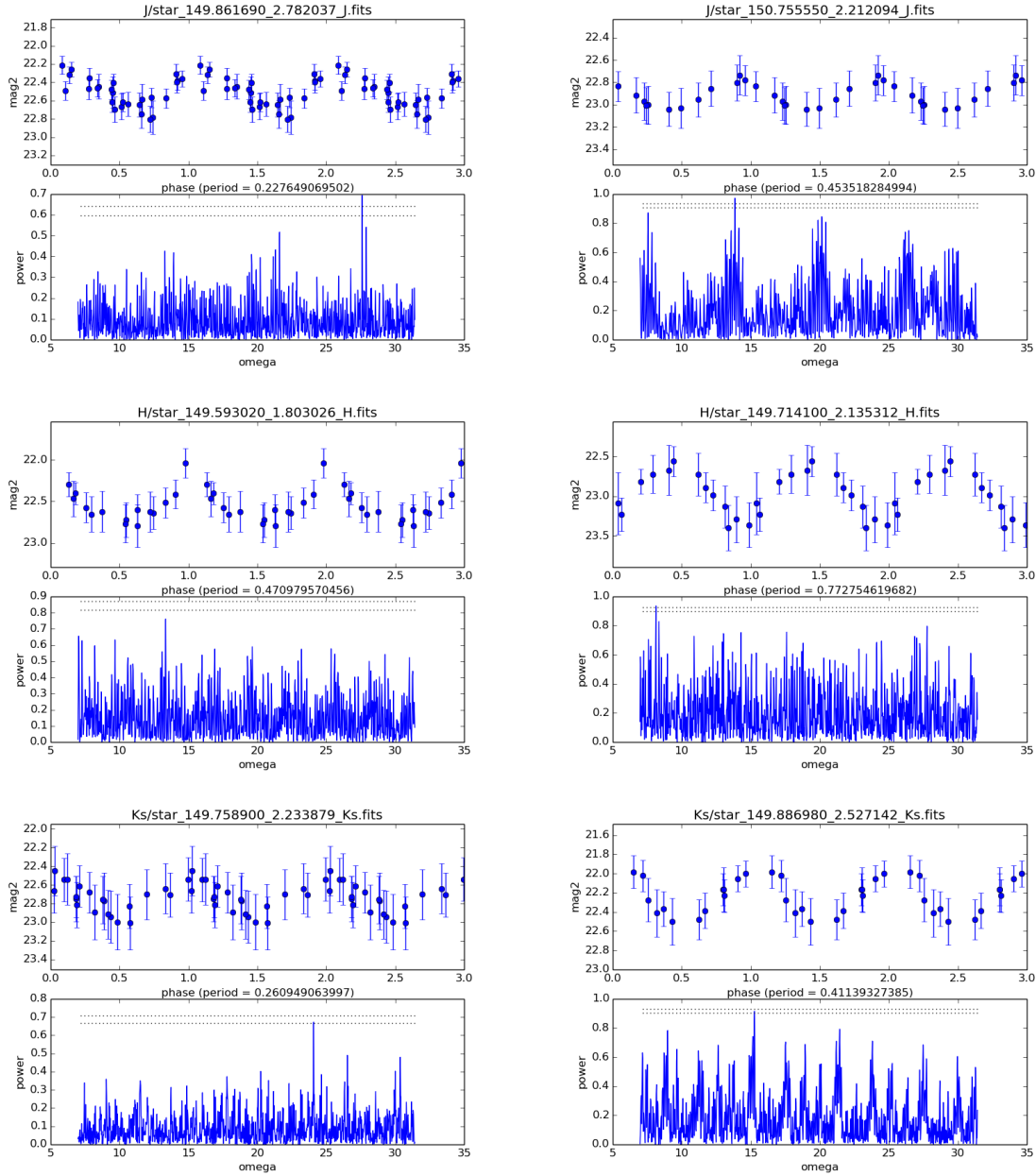


Figure 3.7: Some of the periodograms obtained from UltraVISTA data in the J, H and Ks bands. Above each periodogram is a folded light curve using the observed magnitudes and the period estimated by the Lomb-Scargle periodogram.

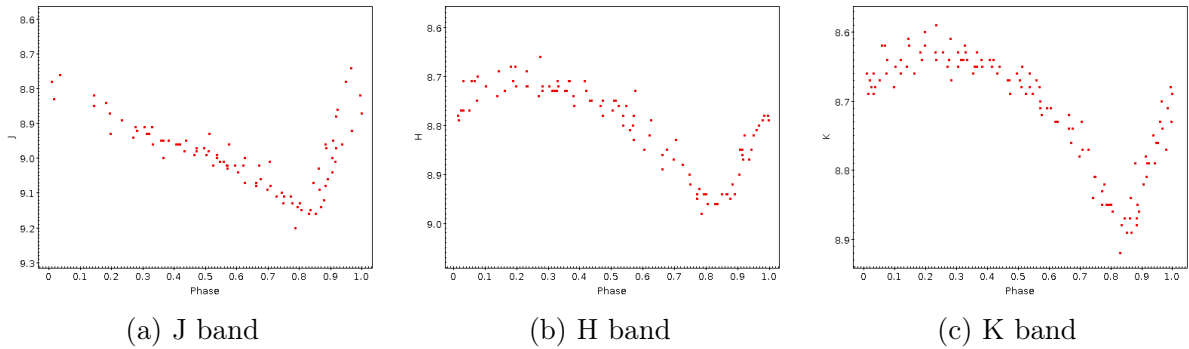


Figure 3.8: The light curves of RR Lyra star DX Del in the H, J and K bands. (data taken from the VVV Templates Project (Angeloni et al., 2014))

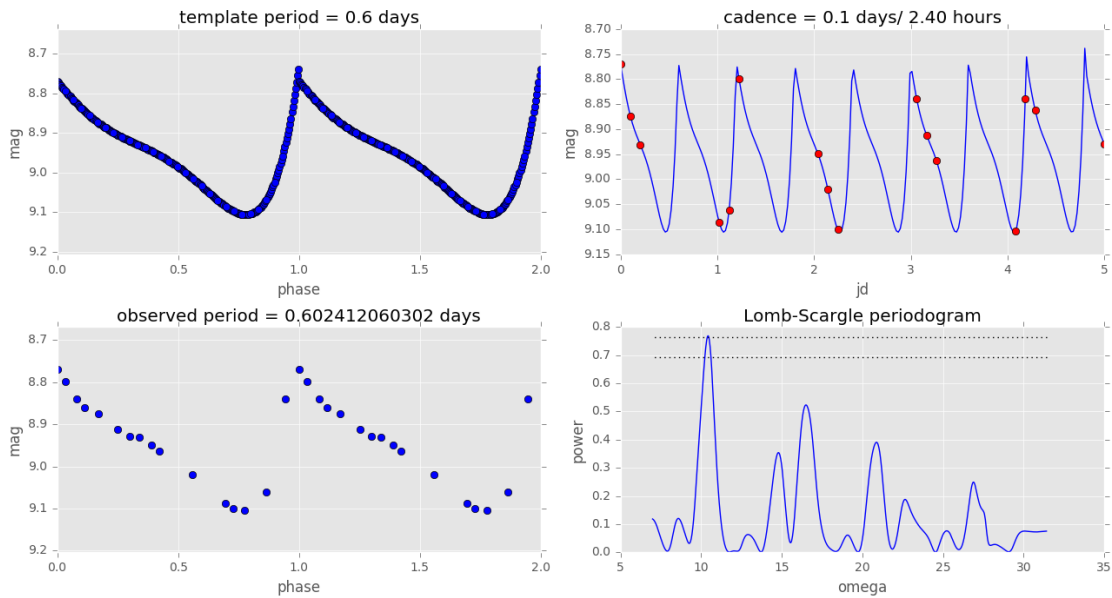
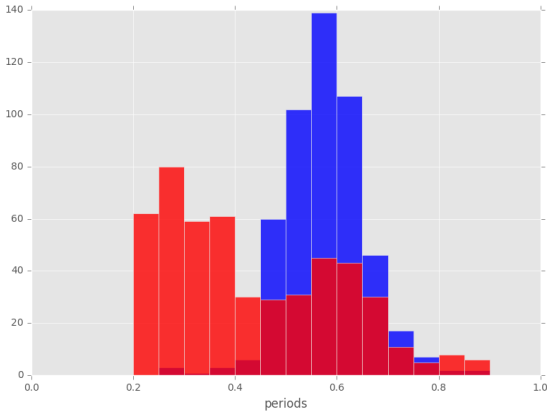
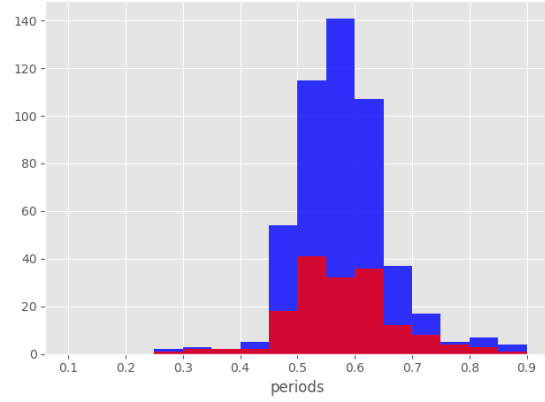


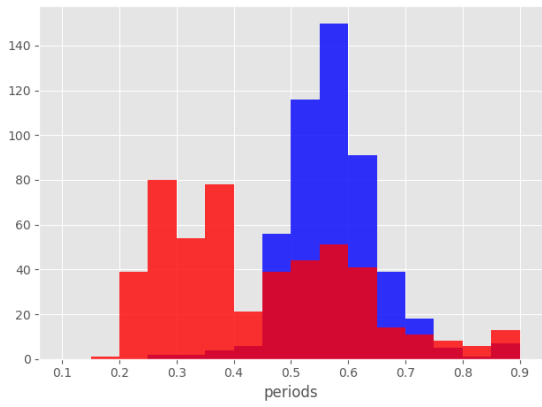
Figure 3.9: An example of a simulated observation of an RR Lyrae template light curve. The top left panel shows the original light curve used from the template. The top right panel shows the light curve repeating periodically in time, with the red dots representing the simulated observations that are taken with the cadence from UltraVISTA. The bottom right panel shows the Lomb-Scargle periodogram that results from the simulated data mentioned previously. Finally, the bottom left panel shows the simulated observations shown in phase, using the estimated period from the Lomb-Scargle periodogram. Since the original period is recovered, we can see a resemblance between the light curves in the bottom and top left panels.



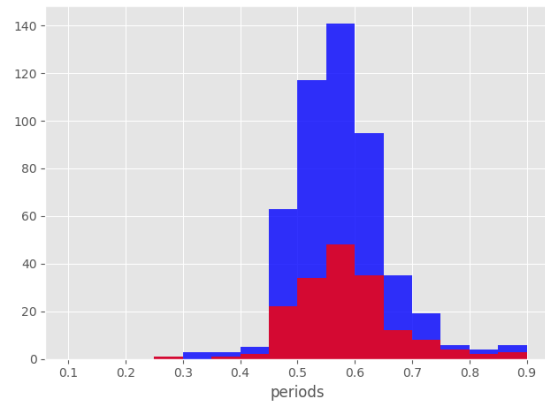
(a) J band (all)



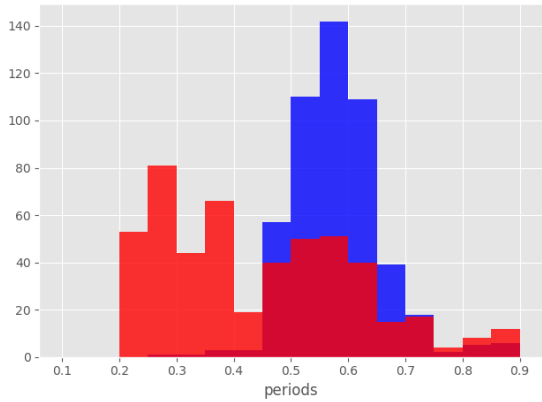
(b) J band (recovered)



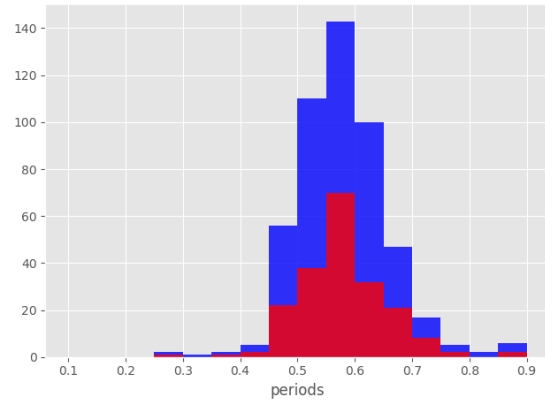
(c) H band (all)



(d) H band (recovered)



(e) K band (all)



(f) K band (recovered)

Figure 3.10: A histogram of period distributions. In blue is the distribution of 500 known RR Lyrae from the Catalina Survey. The distribution in red are the periods from our simulated observations of said stars.

# Chapter 4

## SUDSS

### 4.1 Data

The Search Using DECam for Superluminous Supernovae (SUDSS) (Scovacricchi et al., 2016) is an extension to the Dark Energy Survey (DES (The Dark Energy Survey Collaboration, 2005)) supernovae program. It adds extra epochs at either side of the nominal DES season, and nearly eight months to the original observing window. This is done in order to alleviate some of the temporal edge effects that occur in SNe observation with DES, in which high redshift SNe light curves can be extended to a period longer than the observing window of the survey.

The instrument used for SUDSS is the Dark Energy Camera (DECam), which is mounted on the Blanco 4m telescope at the Cerro Tololo Inter-American Observatory (CTIO). DECam has an array of 62 CCDs arranged in a hexagonal pattern (Figure 4.1), which are specifically designed to observe red light from distant galaxies (DEC). Together, these CCDs cover an area of  $3\text{deg}^2$ . The pixel scale of the images is  $0.26\text{ arcsec/px}$ . DECam works in 8 filters (ugrizY, wide VR, and narrow N964), but for SUDSS data we only have observations in the  $g$  and  $r$  bands.

SUDSS covers 5 different fields with a total of 8 pointings: E1, E2, C3, X3, Cosmos1, Cosmos2, NSF1 and NSF2. I am working with observations from the Elais (also called  $E$ ) field in the  $g$  and  $r$  bands, since it is the field with more observations at long exposures, and is also present in the DES Gold Catalog for a better calibration (see Section 4.1.1). This field has multiple observations with exposures of 100, 130, and 180 seconds in the  $g$  band, while on the  $r$  band it has observations with exposures of 135, 200 and 250 seconds. SUDSS has two pointings observing the E field (from here on referred to as E1 and E2), detailed in Table 4.1.

All observations from SUDSS used in this work are publicly available in the NOAO Science

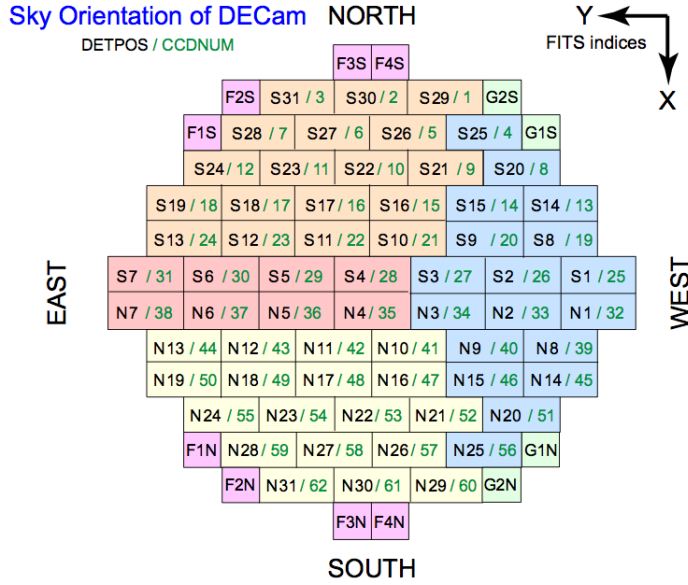


Figure 4.1: The CCD array used in the Dark Energy Camera

Field	RA (h)	DEC (h)	RA (deg)	DEC (deg)
E1	00:31:29.86	-43:00:34.6	7.87440	-43.0096
E2	00:38:00.00	-43:59:52.8	9.50000	-43.9980

Table 4.1: Pointings used to observe the E field in SUDSS

Archive (NOA). The images were flux and astrometrically calibrated by the NOAO pipeline.

### 4.1.1 Catalogues & Calibration

Catalogs of each observations were made using SExtractor (Bertin and Arnouts, 1996) (see Section 3.2), from which I also obtained instrumental magnitudes. These instrumental magnitudes are normalized by exposure time, so images with different exposure times can be compared. To calibrate the photometry of these catalogs, I used the method explained in Cartier et al. (2015), which corrects for possible non-linearities using a linear fit as a function of  $g$ , as it is shown to be a better fit than a constant zeropoint. The fit is defined as:

$$g - g_{DES} = \alpha + \beta \times g \quad (4.1)$$

Where  $g$  is the instrumental magnitude,  $g_{DES}$  is the magnitude from the DES Gold Catalog (DES), and  $\alpha$  and  $\beta$  are constants used for the linear fit. When making this linear fit I exclude sources that are too bright or too faint to avoid distortions in the fit, using only those sources in the middle of each filter’s magnitude range (Table 4.2) where no significant distortions can be found. I also sigma-clip the fit to eliminate outliers from the calibration.

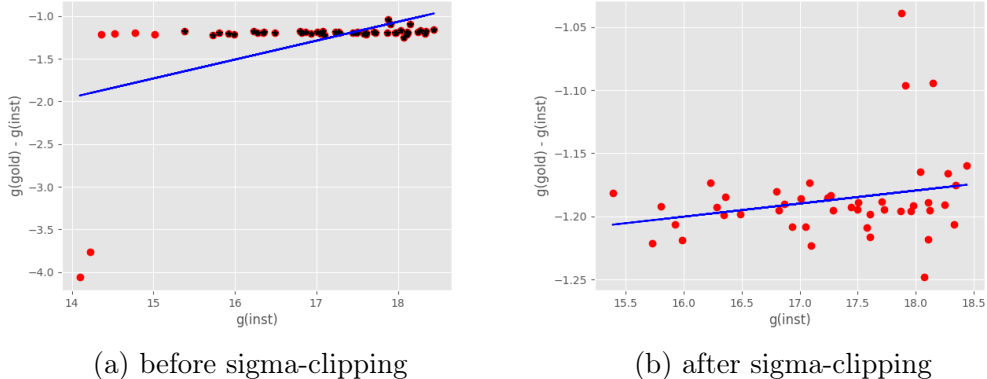


Figure 4.2: Linear fit used for  $\sigma$ -clipping calibration (Equation 4.1)

Exposure time	Objects used
100 s	$14 < g < 18.5$
130 s	$15.5 < g < 21$
180 s	$17 < g < 22$
135 s	$17 < r < 21$
200 s	$18.5 < r < 22$
250 s	$19 < r < 22$

Table 4.2: Magnitude ranges used for photometric calibration.

### 4.1.2 Catalog matching and construction of light curves

To construct the light curves, I match the calibrated catalogs to the DES Gold Catalog (DES). Measurements that have been flagged by SExtractor when creating the catalogs (for errors in the photometry, bad or saturated pixels, among other things) are not considered when constructing the light curves. When calibrating the catalogs I also calculate the  $\chi^2_\nu$  and standard deviation  $\sigma_{fit}$  of the linear fit (following the procedure described in Cartier et al. (2015)). Catalogs with  $\chi^2_\nu < 20$  or  $\sigma_{fit} < 0.1$  are discarded. Since multiple observations are needed to do a time series analysis, only objects with over 10 epochs are exported as light curves to ensure there are enough data points to analyze with the Lomb-Scargle periodogram.

For star-galaxy classification, I use the MODEST\_CLASS classification in the DES Gold Catalog (Jarvis et al., 2016), a classification that is a mix of the star-galaxy classification from SExtractor and the SPREAD\_MODEL measure from Desai et al. (2012). For here onwards I only work with stellar objects (that is, MODEST\_CLASS = 2). This cut can be seen in Figure 4.3, which shows the noise in the data from the  $g$  band as it reaches higher magnitudes. This cut leaves out 19461 objects of the original sample of 33267. The number of epochs for each resulting light curve after all the cuts mentioned above is shown in Figure 4.4.

To focus this search for RR Lyrae even further, a color cut is done at approximately  $g - r \leq 0.25$ , leaving a final sample of 2106 objects to analyze. This cut is shown as the

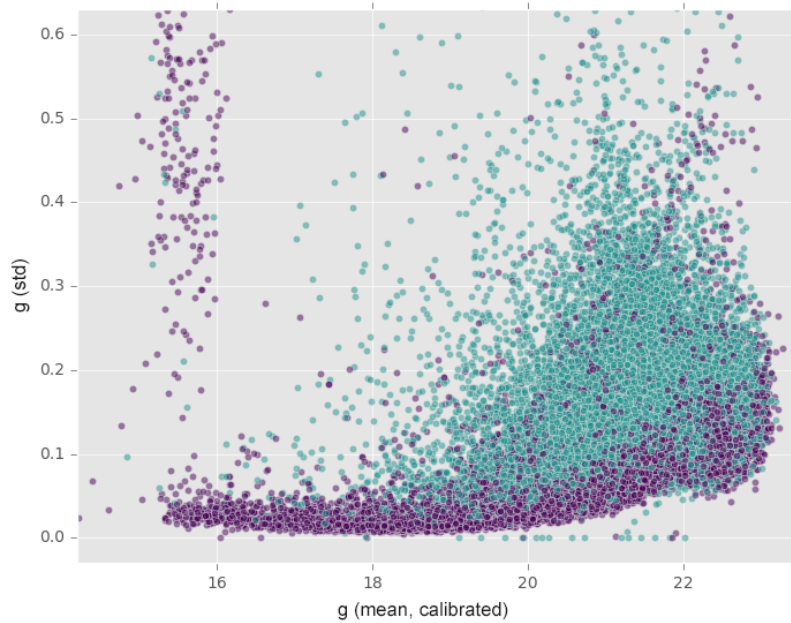


Figure 4.3: All the matched objects with over 10 epochs. Points in teal are classified as galaxies, while points in purple are classified as stars. Stars in the upper left section of the diagram are saturated stars and are not considered for this work.

turquoise area in the color-magnitude diagram of Figure 4.5.

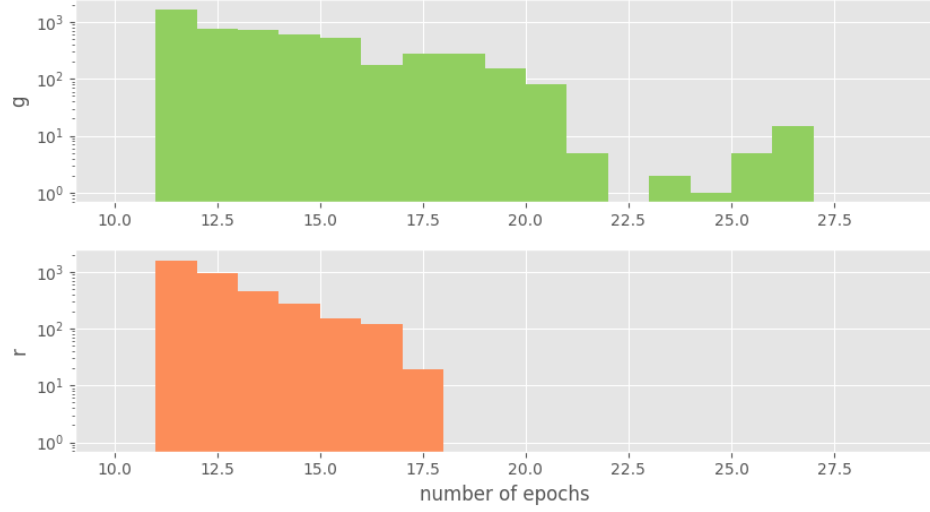


Figure 4.4: Histogram of the number of epochs per light curve in each photometric band, for the light curves selected after the process described in Sections 4.1.1 and 4.1.2.

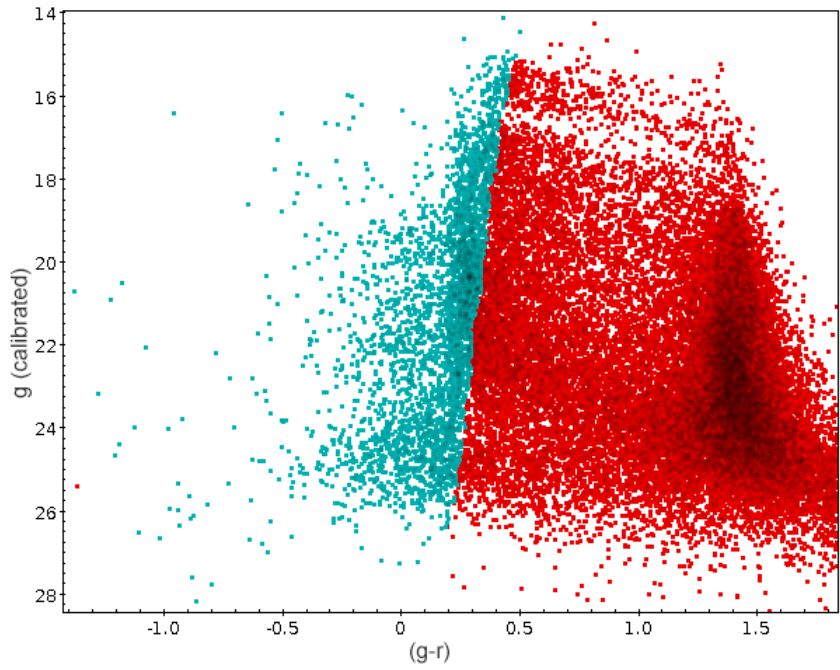


Figure 4.5: A color-magnitude diagram of all observed stars. Stars in blue are selected to look for RR Lyrae.



## 4.2 Results

After constructing the light curves and selecting the possible RR Lyrae candidates, I search for periodic signals using the Lomb-Scargle periodogram. Given the coverage of the observations, and based on previous surveys (Medina et al., 2018; Drake et al., 2013b),  $\sim 8$  RRL were expected to be found in the observed area. However, no RR Lyrae were found.

A distribution of the estimated periods obtained in each band is shown in Figure 4.6. This distribution does not show any specific peaks caused by aliasing. There are more individual peaks in the distribution for the  $r$  filter, which are probably spurious peaks due to the  $r$  band having less epochs in general (see Figure 4.4)

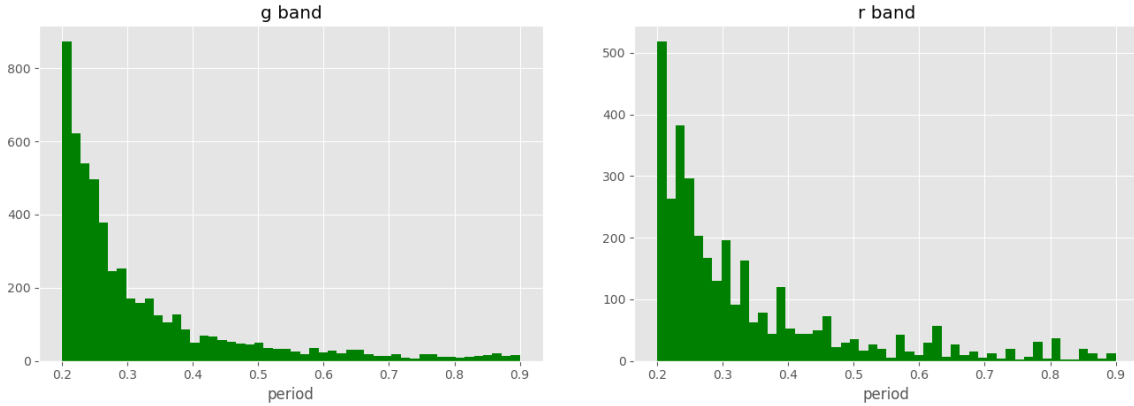


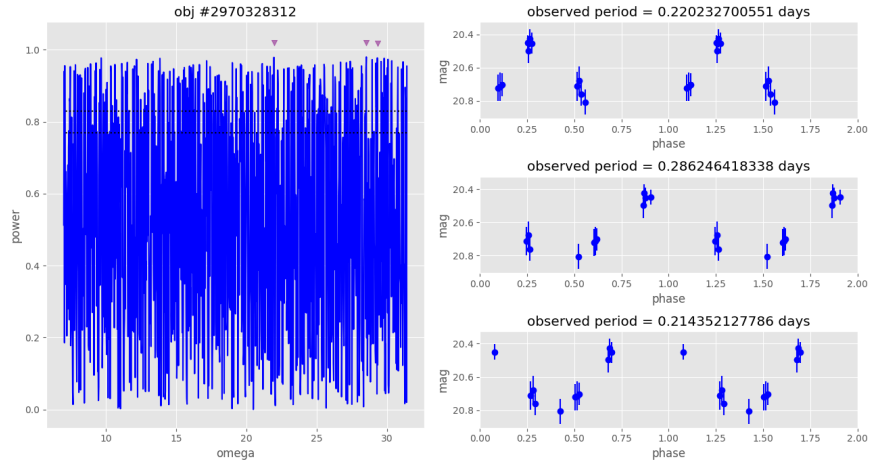
Figure 4.6: Distribution of the periods estimated by the Lomb-Scargle periodogram in the  $g$  and  $r$  bands.

Figure 4.7 shows some examples of periodograms obtained with SUDSS light curves. These periodograms appear to be more noisy than those obtained with UltraVISTA, with no clear peaks to be found. Most periodograms obtained have many peaks that are considered significant by the bootstrapping analysis. This is probably driven by the lower number of epochs of these light curves, which allows for better fits at many different periods.

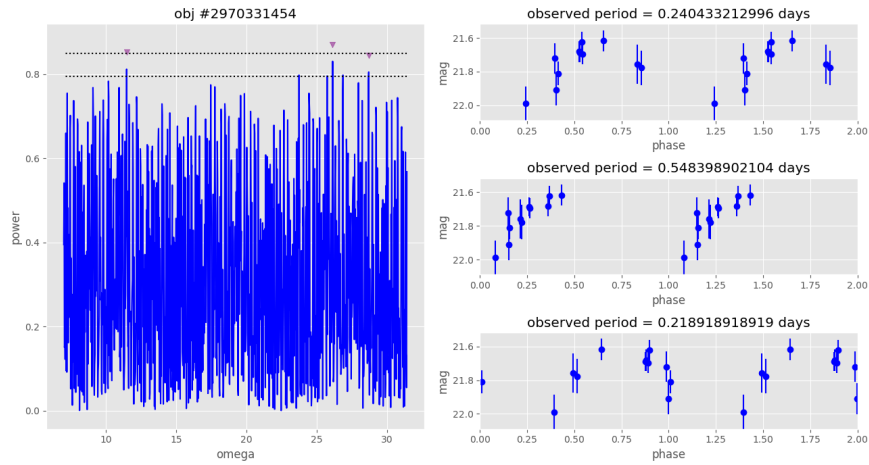
### 4.2.1 Simulating RRL observations to test SUDSS cadence

In order to investigate the null results I test whether the cadence from the SUDSS light curves is suitable for searching for RR Lyrae. For this I run the test described in Section 3.4.1. The distributions obtained for 500 objects in the  $g$  and  $r$  bands are shown in Figure 4.8. The distributions show that using the cadence from SUDSS, the original periods are not recovered. While the original distribution from the Catalina survey shows a clear peak around the period of 0.6 days, the distribution recovered by Lomb-Scargle is more or less uniform with no clear peaks on both the  $g$  and  $r$  bands.

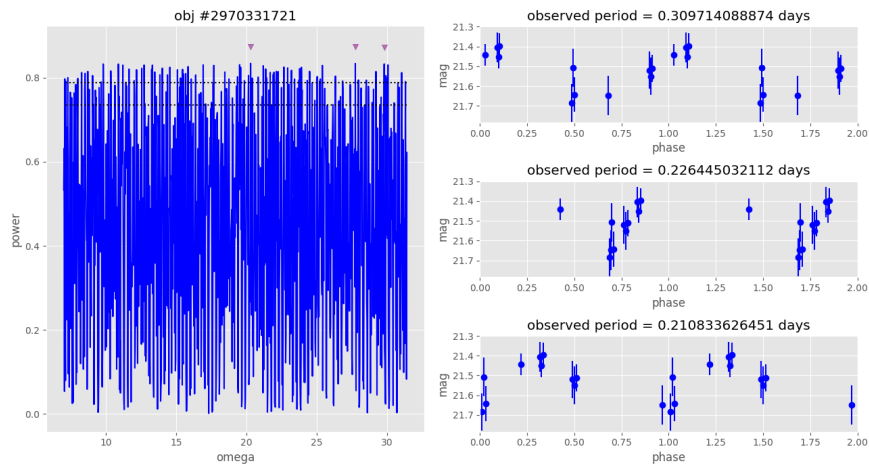
The right side of Figure 4.8 shows, in red, the distribution of the recovered periods. Only 3.8% of the original periods were recovered in the  $g$  band, while 3.0% were recovered in the  $r$  band. This is consistent with the periodograms seen in Figure 4.7, where there are no clear peaks and so it becomes less likely to find the original period.



(a)

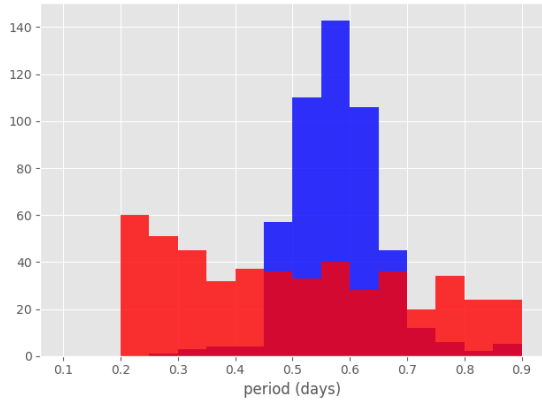


(b)

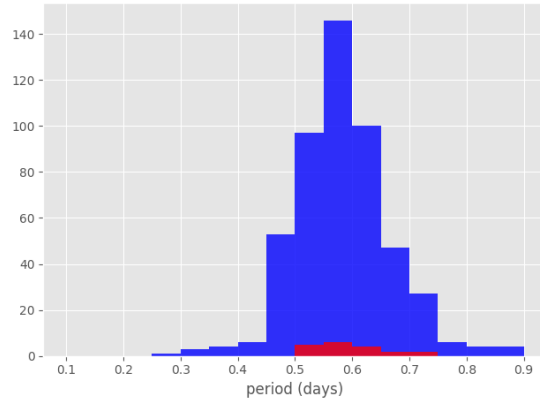


(c)

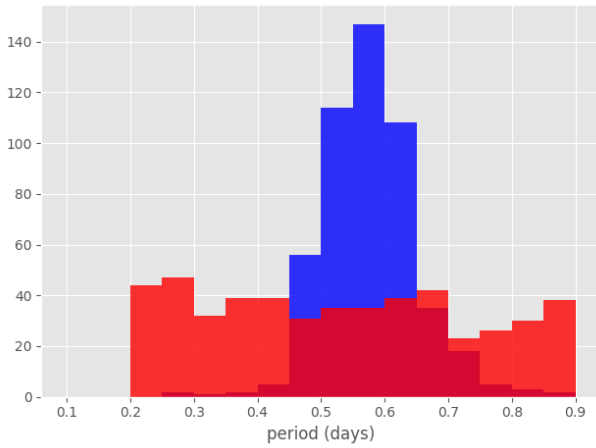
Figure 4.7: Examples of Lomb-Scargle periodograms obtained for different SUDSS objects in the  $g$  band. Each periodogram is on the left side. On the right side are the phased light curves for the 3 highest peaks of the periodogram. The dotted lines in the periodogram show the 10% and 5% significance levels.



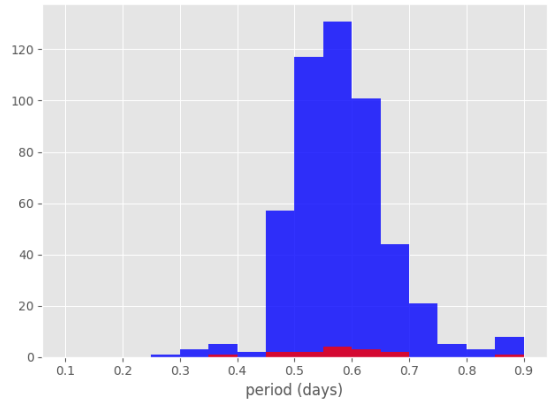
(a) g band (all)



(b) g band (recovered)



(c) r band



(d) r band (recovered)

Figure 4.8: Histograms of period distributions. In blue is the original distribution from the Catalina Survey, while the distribution in red is what is recovered when simulating observations with the same cadence as 500 SUDSS objects (in the  $g$  and  $r$  bands, respectively) chosen at random.

# Chapter 5

## HiTS

In this chapter I introduce a third dataset, which uses data from HiTS 2015A. Here I test the cadence of this survey with simulated observations, and then proceed to analyze the real data in search of distant RR Lyrae.

### 5.1 Data

The High cadence Transient Survey (HiTS) (Förster et al., 2016) is a survey carried out during 2013 to 2015. It is done in the optical range, using the Dark Energy Camera (DECam, see Section 4.1). The original purpose of HiTS is to detect and follow-up optical transients, most specifically the earliest hours of supernovae explosions (shock breakouts).

The cadence of this survey is defined by the characteristic timescales of its main science goal: SNe shock breakouts. SBO timescales range from seconds to a few hours (Kistler et al., 2013), but HiTS is focused on the longest scales among these events: SBOs originated from red supergiant (RSG) stars, which have characteristic timescales of an hour or more. Therefore, the cadences used go from 1.3 to 2 hours (4, 5 or 6 epochs per night).

The campaign consisted mostly in observing blindly selected fields that met certain requirements (such as overall low airmasses and remaining visible throughout the entire night). Cluster and supercluster fields were only observed when they were adjacent to the blind fields, to optimize telescope time. The observed fields are shown in Figure 5.1. In this work I use data from the 2015A campaign.

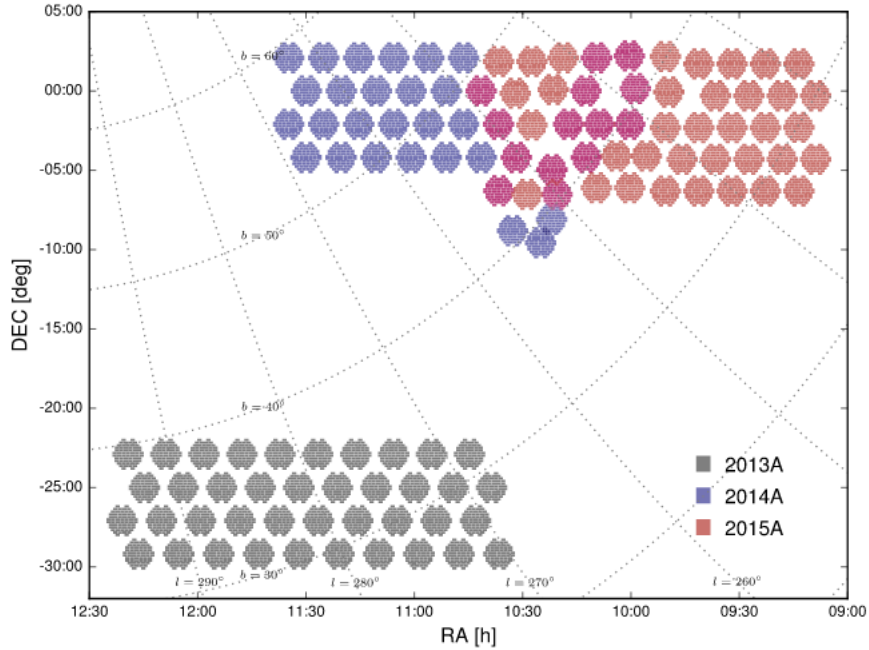


Figure 5.1: The fields observed by HiTS in the campaigns 2013A, 2014A and 2015A, from Förster et al. (2016).

### 5.1.1 Calibration and light curve construction

HiTS worked with a custom process that was designed to run in real-time in order to modify their observational strategies as needed, and to follow-up with other telescopes on the same observing night when new transients were found. This process included readout time, data transfer, expanding the images into individual CCDs, running the DECam community pipeline (Valdes et al., 2014) for preprocessing (electronic bias calibration, cross-talk correction, saturation masking, bad pixel masking and interpolation, bias calibration, linearity correction, flat-field gain calibration, fringe pattern subtraction, bleed trail and edge bleed masking, and interpolation), a CRBlaster filter to remove cosmic rays (Mighell, 2010), and the image subtraction pipeline that detects candidate transients.

The calibration and light curve construction described in this section were carried out entirely by Medina (2017), and the resulting light curves are used in this work with their permission. First, catalogs were created from each image using the SExtractor photometry software. Then these catalogs were aligned with each other, doing a pixel-to-sky coordinate conversion using one of the epochs as a reference frame (the third epoch for 2015A data) and the transformation constants from the HiTS pipeline. The aligned catalogs were then cross-matched to generate light curves, and the measured fluxes were converted into instrumental magnitudes as:

$$g = -2.5 \cdot \log_{10}\left(\frac{\text{counts}}{\text{sec}}\right) - a_g - k_g \cdot A - b_g \cdot ((g - r) - 0, 53) \quad (5.1)$$

Where  $A$  is the airmass,  $a$  is the photometric zeropoint in the respective band and CCD,  $b$  is the instrumental color term coefficient—one for each CCD—and  $k$  is the first-order extinction. This calculation of instrumental magnitudes also accounts for the different exposure times used in the observations.

Finally, these instrumental magnitudes were compared to the reference frame. After filtering those objects within  $2\sigma$ , the median value of this magnitude difference was used as the zeropoint for photometric calibration  $\Delta g_{rel}$  as:

$$g_{ref} = g_{std} + \Delta g_{rel} \quad (5.2)$$

## 5.2 Results

First I ran the test described in Section 3.4.1 for 500 objects selected randomly, to test whether the cadence of these observations was suitable for searching for RR Lyrae. The recovered distribution is shown in Figure 5.2. In this case it is clear that the original period distribution is accurately recovered. Checking individual simulations, it is seen that the original periods are recovered on 92.8% of the simulations done using the HiTS data cadence.

After successfully testing the cadence, I searched for RR Lyrae using the real HiTS data. Figure 5.3 shows an example of the resulting periodograms. Compared to the two previous datasets, these periodograms show clear peaks that pass the significance threshold, any many of them show folded light curves that clearly resemble those of RR Lyrae.

We found a total of 106 RR Lyrae. A list of all the RRL, their characteristics and light curves, are detailed in Appendix A. Of all the RR Lyrae found, 84 of them are RRab (79.25%) and 22 are RRC (20.75%), which matches with the distribution expected from the literature ( $\sim 90\%$  RRab and  $\sim 10\%$  RRC) (Smith, 2004). The period-amplitude diagram for these stars is on Figure 5.4, where the expected separation between RRab and RRC stars is clearly defined.

The absolute magnitude values  $M_g$  of the found RR Lyrae were computed using the PLZ relations from Sesar et al. (2017):

$$M = a \log(P/P_{ref}) + b([Fe/H] - [Fe/H]_{ref}) + M_{ref} + \varepsilon \quad (5.3)$$

Where the values  $M_{ref}$ ,  $P_{ref}$ ,  $[Fe/H]_{ref}$ ,  $a$ ,  $b$ , and  $\varepsilon$  are parameters that are constrained in the same work. Note that for the PLZ relation to be applied on RRC stars, its period has to be "fundamentalized" (Dall'Ora et al., 2004) as:

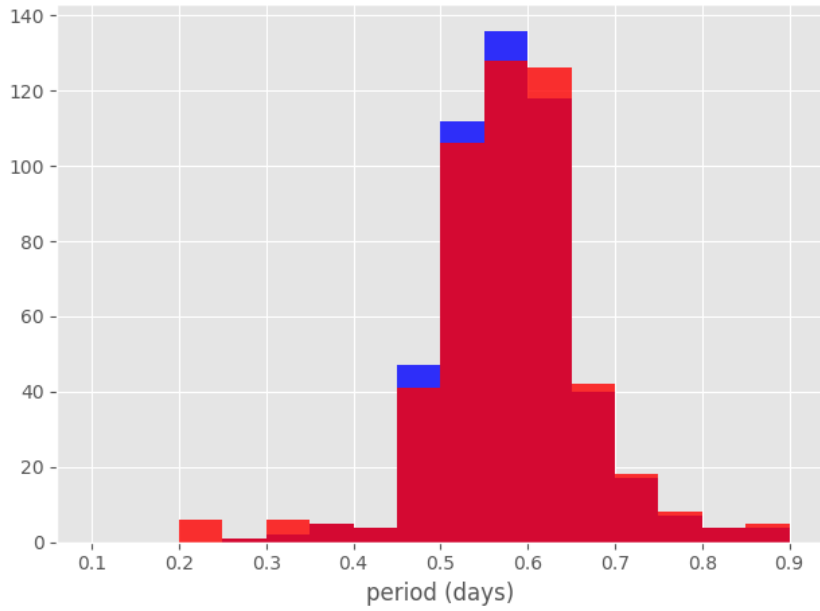


Figure 5.2: A histogram of period distributions. In blue is the original distribution from the Catalina survey, while the recovered distribution using the cadence from HiTS data is shown in red.

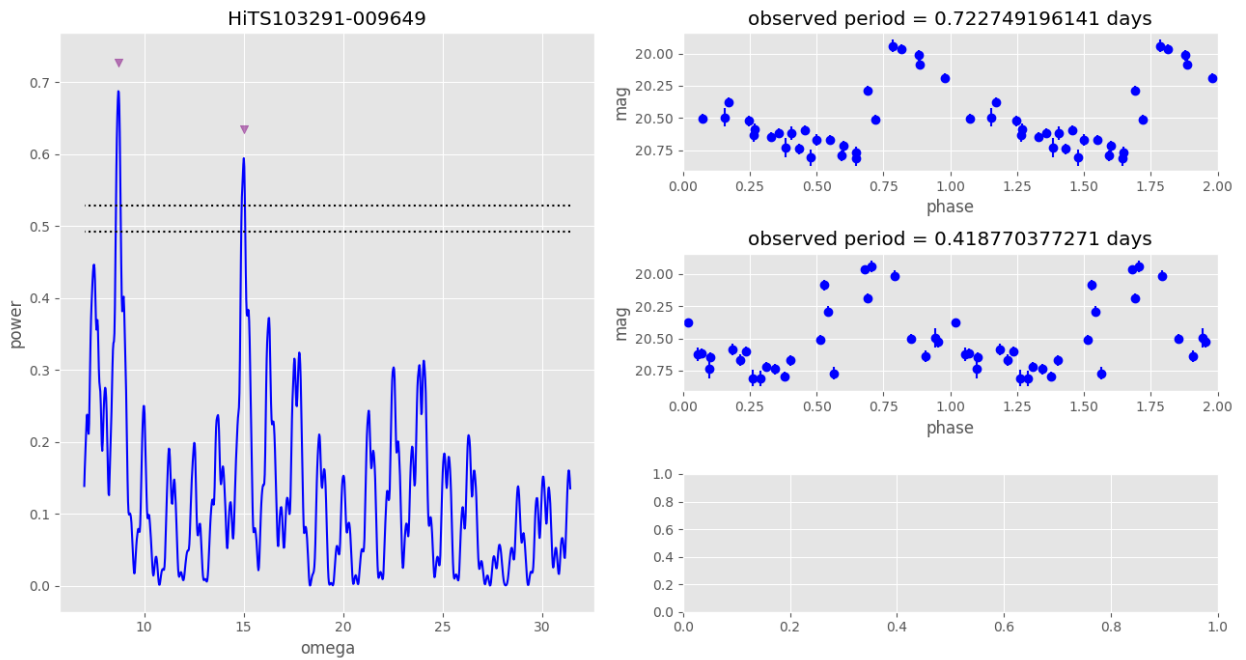


Figure 5.3: An example of one the periodograms obtained with HiTS data, next to their respective phased light curves for the highest peaks.



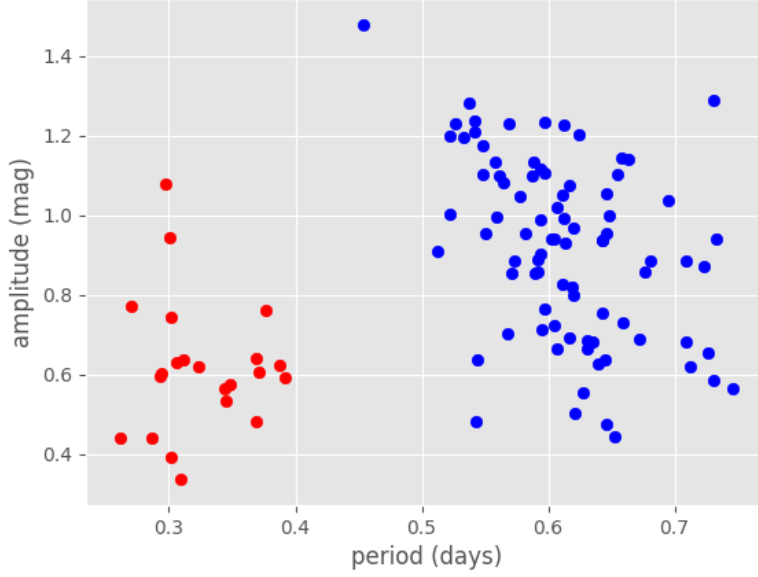


Figure 5.4: Period-amplitude diagram for the RRL found with HiTS data. RRab are shown in blue, and RRc are shown in red.

$$\log P_F = \log P + 0.128 \quad (5.4)$$

Where  $P_F$  is the fundamentalized period used in the PLZ relation, and  $P$  is the original period of the RRc. Once the absolute magnitude  $M_g$  has been obtained, I estimate the heliocentric distances using the distance modulus (Equation 1.5), accounting for the effect of extinction on the measured apparent magnitude:

$$d = 10^{(m-M-A_\lambda+5)/5} = d'10^{A_\lambda/5} \quad (5.5)$$

Where  $A_\lambda$  is the extinction in magnitudes, and  $d'$  is the estimated distance neglecting the effect of extinction.

Figure 5.5 shows the position of the 106 RR Lyrae found in this work, color coded by their heliocentric distance (these distances are listed individually in Appendix A). RRL from the Sextans dSph can be identified around  $RA \simeq 153.3^\circ$ ,  $DEC \simeq -1.7^\circ$  and  $d_H \simeq 80kpc$ , in accordance to the results in Medina et al. (2018).

Of all the RR Lyrae found in this work, 19 were found at a distance of over 90kpc (what can be considered "distant RR Lyrae"): 17 RRab (89.47%) and 2 RRc (10.53%). Of these 19 stars, 7 were found at distances greater than 100 kpc—5 RRab (71.43%) and 2 RRc (28.57%).

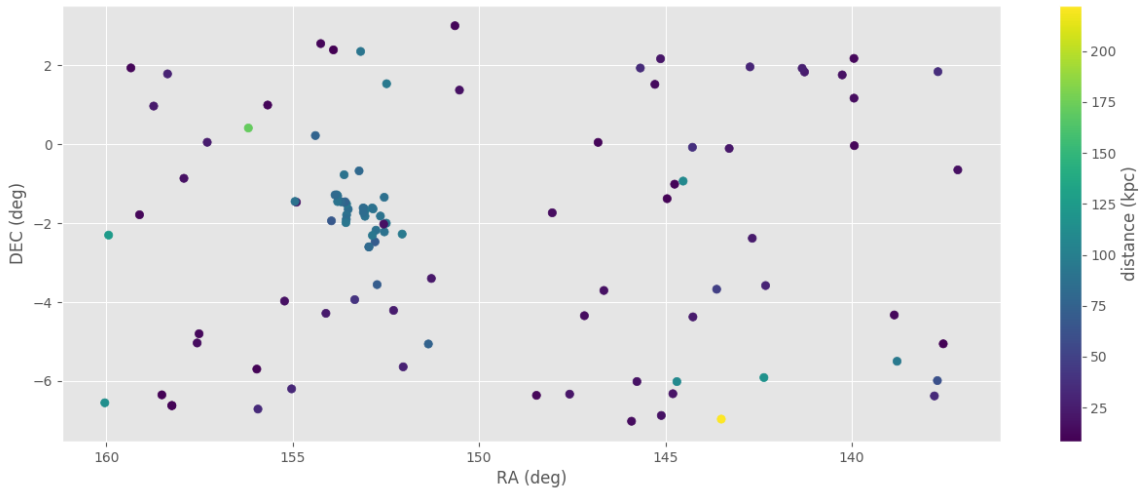


Figure 5.5: Distribution of the found RRL, color coded by heliocentric distance.

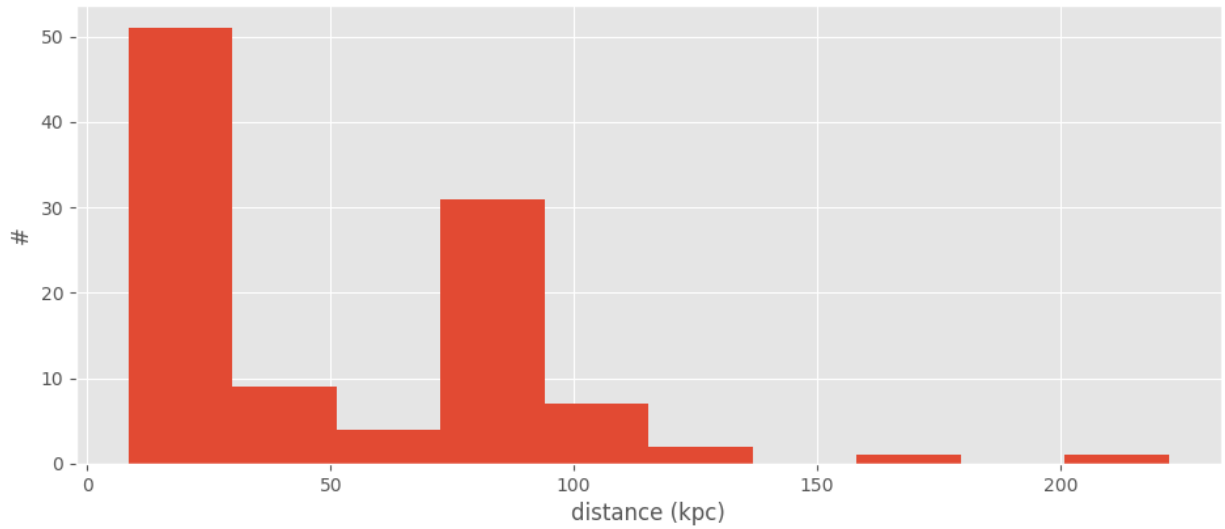


Figure 5.6: Histogram of the heliocentric distances of the found RRL.

# Chapter 6

## Discussion

The main goal of this work was to search for RR Lyrae beyond the usual limit of  $d \sim 100 \text{ kpc}$  where their density seems to drop drastically (Drake et al., 2013a), with the primary aim of building a catalog of distant mass tracers of the Milky Way. For this purpose we exploited three different photometric surveys; UltraVISTA, SUDSS, and HiTS, all deep enough to uncover RRL out to  $\sim 250 \text{ kpc}$ , should they exist.

The null results from UltraVISTA and SUDSS—and their respective simulated observations—show that, despite having good data (observations with small errors and high magnitudes), cadence plays a vital role when analyzing time series to search for RR Lyrae. The cadence in these observations caused a larger amount of noise in the Lomb-Scargle periodogram, which made it impossible to find the true period of the stars observed (if they were, in fact, periodic).

More successful was the search using the HiTS database. In this catalog we found 106 RR Lyrae, 7 of which were detected at distances greater than  $100 \text{ kpc}$ , with the most distant one located at  $\sim 220 \text{ kpc}$ . These results prove that HiTS is an unprecedented probe of the outer areas of the Milky Way halo. Looking at the position of the found HiTS RRL in the sky they are spread out in a roughly uniform way, which is consistent with the preliminary results of Medina (2017). We also find a considerable number of RRL from the Sextans dSph, seen as an overdensity in the amount of RRL in the  $RA \simeq 153.3^\circ$ ,  $DEC \simeq -1.7^\circ$  and  $d_H \simeq 80 \text{ kpc}$  area.

Finding RRL at these distances is a major breakthrough in the context of solving some of the issues posed in Chapter 1.2.1, such as estimating the mass of the Milky Way by tracing the kinematics of these distant stars. It also shows that faint satellites could be detected by observing overdensities of RRL, which opens the possibility of faint Milky Way satellites that have not been found yet to be discovered with this technique.

The RRL detected at large distances correspond to a density of  $0.05 \text{ RRL}/\text{deg}^2$  beyond  $100 \text{ kpc}$ , similar to the results from Medina (2017), which estimate  $0.06 \text{ RRL}/\text{deg}^2$  beyond

100 kpc. These numbers suggest that there be could up to  $\sim 2000 - 2400$  total RRL in the outskirts of the Milky Way ( $d > 100$  kpc), greatly improving our prospects of finding very distant mass tracers.

In this context, studies like this one are an important predecessor for the advent of the Large Synoptic Survey Telescope, LSST (LSST Science Collaboration et al., 2009). LSST aims to have a deep, wide coverage of the sky, using a  $9.6 \text{ deg}^2$  camera to survey up to  $20,000 \text{ deg}^2$  over its 10-year run. This survey will be able to observe Milky Way satellites at up to  $\sim 400 \text{ kpc}$  (Ivezic et al., 2008; Oluseyi et al., 2012). Current works searching for RR Lyrae will help develop the techniques necessary to take on the large amounts of data that will come with LSST.

# Conclusion

RRL are variable stars, key for distance estimations and studies of old stellar populations. They can be found by obtaining light curves and estimating their periods with the Lomb-Scargle periodogram.

This work considered data sets from 3 different surveys: UltraVISTA, SUDSS and HiTS. UltraVISTA worked in the near infrared and reached up to an average of 22 magnitudes, with a small variation for each band. Possible candidates were selected by a variability criteria based on the  $\chi^2$  value of the light curves and the excess variance  $\sigma_{rms}^2$ . However, no RRL were found due to the cadence of the survey not being suitable for this search. The effect of aliasing could be observed in the distribution of periods, particularly around 0.25, 0.3 and 0.5 days. By simulating RRL observations we recovered between 32.4 and 39.8% of the periods, depending on the band. However, this was not enough to find RR Lyrae in the real dataset, which only covered  $1.5\text{deg}^2$ .

The second dataset was from SUDSS, an extension of DES with observations in the optical  $g$  and  $r$  bands. Star-galaxy classifications and color cuts were used to constrain the sample for RRL candidates. However, in this case the simulated observations done to test the cadence recovered only 3.8 and 3.0% of the periods in the  $g$  and  $r$  bands, respectively, proving unusable to search for RR Lyrae.

The last analyzed dataset was from HiTS (this work only used data in the  $g$  band), based on the work of Medina (Medina, 2017). In this case 92.8% of the periods are recovered in the simulated observations, proving the cadence is adequate to search for RR Lyrae. Analyzing the data from HiTS 2015A we find a total of 106 RR Lyrae—84 RRab and 22 RRc. Of these RRL, 7 are at distances larger than 100 kpc, proving to be consistent with what we expect from the literature. Some of these stars belong to the Sextans dSph, located at a distance of  $\sim 80\text{kpc}$ . These findings—especially those of distant RR Lyrae—are proof that distant halo stars can be found with these methods, allowing us to advance in some of the issues currently discussed in Galactic Astronomy, and paving the way for the work to be done with bigger surveys coming in the near future.

# Appendix A

## HiTS 2015a RRL

This appendix contains the full list of RRL found from HiTS data (Chapter 5) and their respective light curves.

Table A.1: RRLs found with HiTS 2015a

ID	RA (deg)	DEC (deg)	$\langle g \rangle$	period	amplitude	$d_H$	type
HiTS100351+00917	150.5274	1.3755	16.88	0.73	0.94	17.84	ab
HiTS100432+020044	150.6485	3.0067	16.08	0.61	0.94	11.58	ab
HiTS100853-022658	151.2805	-3.3987	17.67	0.51	0.91	22.40	ab
HiTS100907-033731	151.361	-5.0597	20.18	0.62	0.69	75.35	ab
HiTS101357-037597	152.0363	-5.6396	18.08	0.55	1.10	27.65	ab
HiTS101376-015158	152.064	-2.2737	20.62	0.70	1.04	95.73	ab
HiTS101529-028056	152.2946	-4.2084	17.98	0.38	0.76	24.37	c
HiTS101654+010244	152.4815	1.5367	20.67	0.62	0.50	94.93	ab
HiTS101659-013322	152.4899	-1.9983	20.58	0.65	1.00	91.16	ab
HiTS101694-014783	152.5415	-2.2175	20.49	0.67	0.69	89.08	ab
HiTS101696-008941	152.5445	-1.3412	20.43	0.68	0.89	86.40	ab
HiTS101706-01347	152.5594	-2.0205	17.03	0.56	1.00	16.84	ab
HiTS101764-012116	152.6473	-1.8174	20.46	0.73	0.65	89.50	ab
HiTS101824-0237	152.7361	-3.555	19.99	0.64	0.76	70.50	ab
HiTS101844-014503	152.7664	-2.1755	20.54	0.59	0.90	87.53	ab
HiTS101861-016466	152.7918	-2.4699	20.43	0.31	0.63	69.93	c
HiTS101896-010914	152.8445	-1.6372	20.64	0.61	0.72	91.31	ab
HiTS101908-015394	152.8622	-2.3092	20.53	0.71	0.62	92.99	ab
HiTS101911-010746	152.8674	-1.612	20.57	0.59	0.99	87.80	ab
HiTS101970-017327	152.9559	-2.5991	20.30	0.64	0.94	81.34	ab
HiTS101970-017327	152.9559	-2.5991	20.30	0.64	0.94	81.34	ab
HiTS102038-0112	153.0578	-1.68	20.75	0.61	0.67	95.06	ab
HiTS102040-012147	153.0612	-1.8221	20.51	0.66	0.73	88.79	ab
HiTS102057-010836	153.0855	-1.6255	20.62	0.71	0.89	93.89	ab
HiTS102070-011477	153.1054	-1.7216	20.52	0.57	1.23	83.97	ab

Table A.1 – continued from previous page

ID	RA (deg)	DEC (deg)	$\langle g \rangle$	period	amplitude	$d_H$	type
HiTS102073-010746	153.1106	-1.612	20.50	0.59	1.10	83.53	ab
HiTS102118+0157	153.1776	2.355	20.73	0.53	1.20	91.62	ab
HiTS102146-004480	153.2195	-0.6721	20.29	0.65	1.05	80.33	ab
HiTS102224-026239	153.3361	-3.9359	18.88	0.58	0.95	40.89	ab
HiTS102340-010972	153.5107	-1.6458	20.52	0.54	1.21	83.81	ab
HiTS102369-011906	153.5544	-1.7859	20.51	0.61	0.93	87.31	ab
HiTS102370-010063	153.5563	-1.5095	20.61	0.64	0.68	92.31	ab
HiTS102375-012664	153.5629	-1.8997	20.42	0.61	1.23	83.68	ab
HiTS102381-013232	153.5725	-1.9848	20.66	0.59	1.12	92.56	ab
HiTS102395-009706	153.5938	-1.4559	20.54	0.34	0.56	75.97	c
HiTS102413-005135	153.6205	-0.7703	20.56	0.63	0.66	89.82	ab
HiTS102463-009711	153.6953	-1.4567	20.63	0.37	0.64	81.12	c
HiTS102529-008714	153.7947	-1.3071	20.27	0.73	0.59	82.70	ab
HiTS102530-009666	153.7954	-1.45	20.60	0.61	1.02	90.50	ab
HiTS102543-008536	153.8151	-1.2804	20.45	0.73	1.29	89.83	ab
HiTS102576-008546	153.8643	-1.2819	20.42	0.57	0.88	81.48	ab
HiTS102604+015966	153.9073	2.3949	15.84	0.31	0.64	8.42	c
HiTS102640-012923	153.9606	-1.9385	20.31	0.32	0.62	66.97	c
HiTS102739-028552	154.1091	-4.2828	17.54	0.75	0.57	23.69	ab
HiTS102832+017026	154.2481	2.554	16.18	0.57	0.70	11.57	ab
HiTS102927+001485	154.3912	0.2228	20.51	0.37	0.61	76.86	c
HiTS103266-009768	154.8997	-1.4652	17.11	0.63	0.55	17.69	ab
HiTS103291-009649	154.9373	-1.4474	20.51	0.72	0.87	89.15	ab
HiTS103352-041316	155.0288	-6.1975	18.36	0.62	0.80	32.33	ab
HiTS103479-026482	155.2185	-3.9723	17.51	0.30	0.39	17.84	c
HiTS103780+006644	155.6709	0.9967	16.40	0.35	0.58	11.13	c
HiTS103954-044728	155.9321	-6.7092	18.40	0.65	0.44	33.82	ab
HiTS103974-037973	155.9623	-5.696	15.90	0.65	0.96	10.61	ab
HiTS104125+002762	156.1888	0.4144	22.44	0.30	0.94	171.54	c
HiTS104861+000352	157.2918	0.0528	17.83	0.64	0.63	24.93	ab
HiTS105007-032005	157.5108	-4.8008	16.41	0.56	1.13	12.80	ab
HiTS105041-033561	157.5626	-5.0342	17.16	0.30	0.74	15.37	c
HiTS105278-00574	157.9172	-0.861	17.60	0.29	0.60	17.84	c
HiTS105493-044139	158.2403	-6.6209	15.67	0.62	1.07	9.41	ab
HiTS105493-044139	158.2404	-6.6209	15.85	0.61	0.99	10.18	ab
HiTS105570+011907	158.3561	1.7861	18.04	0.68	0.86	29.05	ab
HiTS105672-04233	158.5085	-6.3495	15.76	0.55	0.96	9.41	ab
HiTS105818+00647	158.728	0.9705	17.88	0.45	1.48	22.90	ab
HiTS106071-011894	159.1078	-1.7842	16.39	0.60	1.23	12.54	ab
HiTS106226+012918	159.3392	1.9378	16.19	0.65	1.10	12.36	ab
HiTS106624-015336	159.9369	-2.3005	21.23	0.71	0.68	124.67	ab
HiTS106692-043672	160.0389	-6.5509	21.08	0.64	0.64	114.16	ab
HiTS914413-004312	137.162	-0.6469	17.22	0.37	0.48	17.18	c
HiTS917015-033704	137.5523	-5.0557	15.79	0.54	1.24	9.71	ab
HiTS917966+012282	137.695	1.8424	18.56	0.60	0.94	36.10	ab

Table A.1 – continued from previous page

ID	RA (deg)	DEC (deg)	$\langle g \rangle$	period	amplitude	$d_H$	type
HiTS918062-03992	137.7094	-5.988	19.69	0.65	0.47	61.78	ab
HiTS918599-042513	137.7899	-6.377	18.50	0.57	0.85	34.07	ab
HiTS925276-036652	138.7914	-5.4979	20.67	0.62	0.97	94.54	ab
HiTS925773-028830	138.866	-4.3246	16.57	0.39	0.62	12.89	c
HiTS932915-000216	139.9373	-0.0324	16.26	0.61	1.05	12.49	ab
HiTS932973+007806	139.946	1.171	16.70	0.66	1.14	15.86	ab
HiTS932988+014520	139.9482	2.1781	16.75	0.29	0.60	12.82	c
HiTS935079+011737	140.2619	1.7606	17.00	0.62	0.82	17.64	ab
HiTS941816+012231	141.2725	1.8347	18.17	0.34	0.53	25.10	c
HiTS942243+012855	141.3365	1.9283	18.49	0.27	0.77	26.91	c
HiTS948784-023860	142.3177	-3.5791	18.58	0.29	0.44	29.31	c
HiTS949078-039408	142.3618	-5.9112	21.19	0.58	1.05	116.66	ab
HiTS951161-015866	142.6742	-2.38	17.74	0.59	1.13	24.03	ab
HiTS951568+013094	142.7353	1.9642	18.45	0.59	0.86	31.11	ab
HiTS955289-000689	143.2934	-0.1034	17.53	0.62	1.20	22.40	ab
HiTS956703-046427	143.5055	-6.9641	22.96	0.30	1.08	222.31	c
HiTS957527-024481	143.6291	-3.6722	19.29	0.56	1.10	48.05	ab
HiTS961774-029154	144.2661	-4.3732	17.70	0.59	0.89	23.65	ab
HiTS961856-000491	144.2785	-0.0737	18.73	0.60	0.77	37.85	ab
HiTS963526-006207	144.5289	-0.9311	20.96	0.61	0.83	109.38	ab
HiTS964643-04009	144.6965	-6.0135	20.99	0.59	0.85	109.39	ab
HiTS965048-006730	144.7573	-1.0096	16.15	0.60	1.10	11.71	ab
HiTS965356-042138	144.8035	-6.3208	17.33	0.53	1.23	19.58	ab
HiTS966385-009178	144.9578	-1.3768	15.94	0.54	0.64	10.41	ab
HiTS967424-045813	145.1136	-6.872	17.10	0.63	0.69	18.65	ab
HiTS967562+014466	145.1344	2.1699	17.53	0.60	0.71	21.65	ab
HiTS968574+010144	145.2862	1.5216	17.06	0.31	0.34	14.07	c
HiTS971177+012898	145.6766	1.9347	18.71	0.52	1.00	34.63	ab
HiTS971784-040078	145.7677	-6.0118	17.27	0.54	1.28	18.94	ab
HiTS972749-046786	145.9124	-7.018	16.79	0.55	1.17	15.36	ab
HiTS977694-024690	146.6542	-3.7036	17.32	0.39	0.59	17.97	c
HiTS978730+000333	146.8096	0.05	16.54	0.54	0.48	11.41	ab
HiTS981178-028954	147.1767	-4.3431	16.68	0.66	1.14	15.15	ab
HiTS983814-042208	147.5721	-6.3312	17.98	0.26	0.44	20.38	c
HiTS986923-011562	148.0385	-1.7344	16.91	0.52	1.20	15.55	ab
HiTS989747-042410	148.4621	-6.3616	16.37	0.56	1.08	12.24	ab



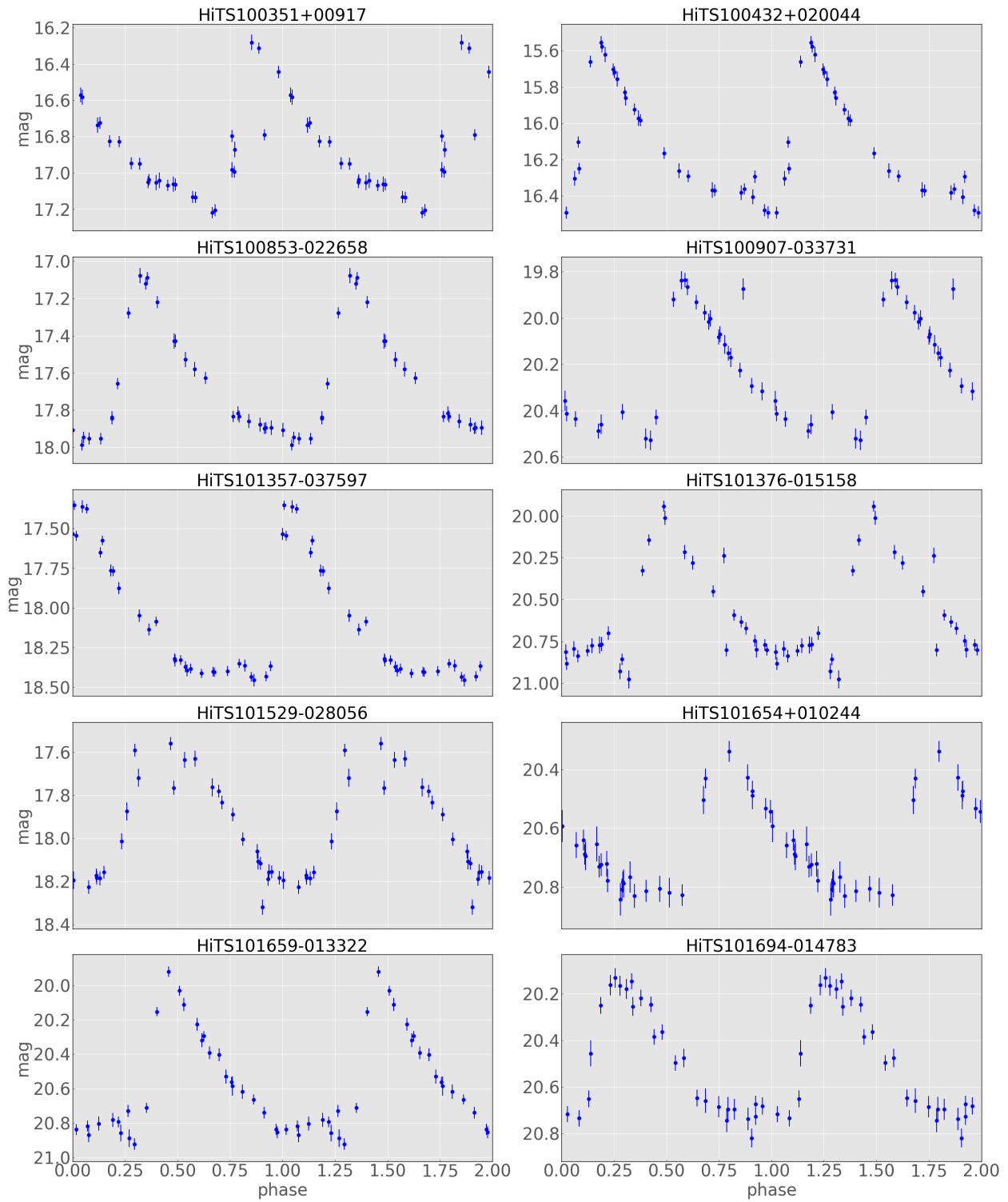


Figure A.1: Phased light curves of RR Lyrae found from HiTS 2015a (1/11)

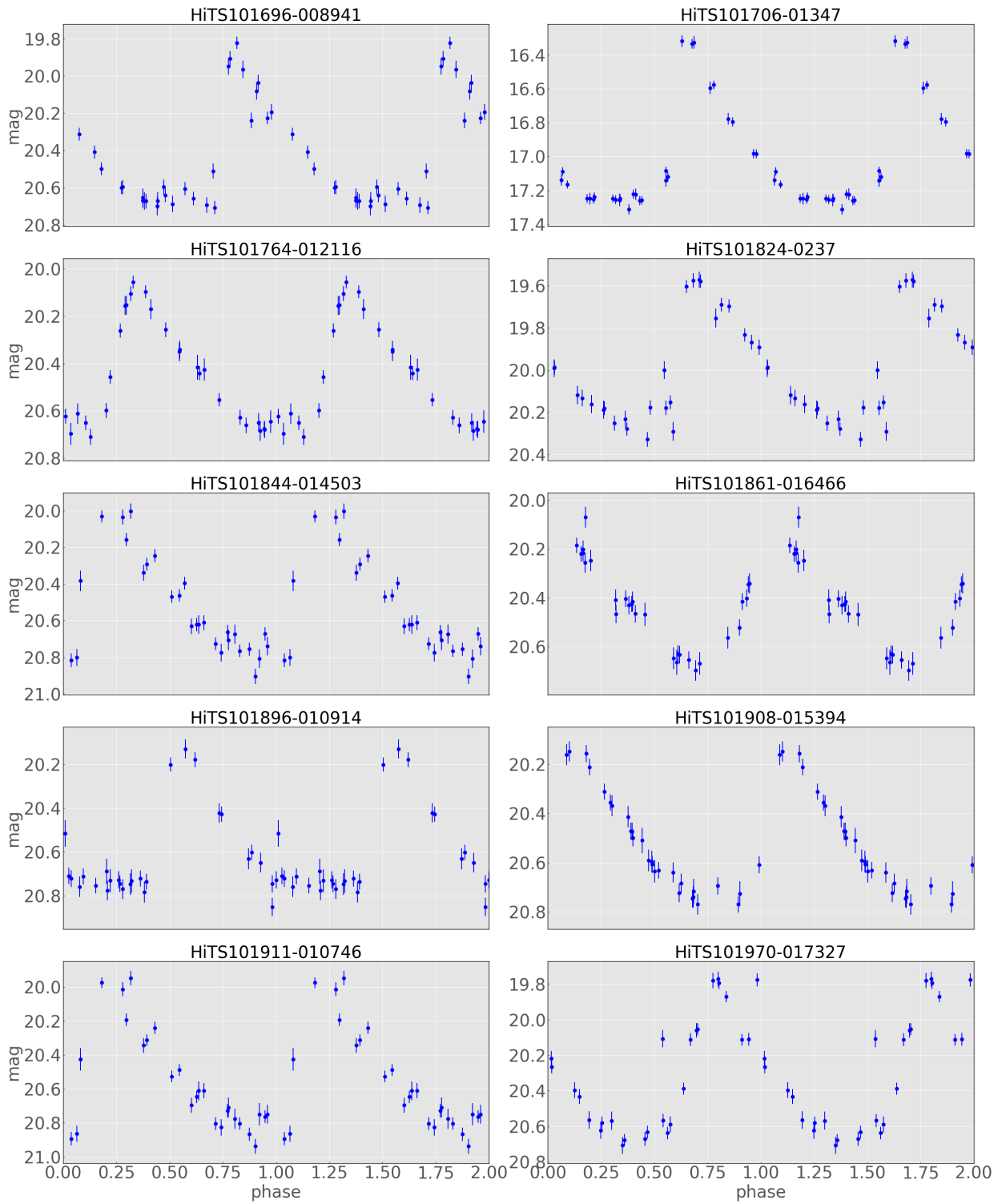


Figure A.2: Phased light curves of RR Lyrae found from HiTS 2015a (2/11)

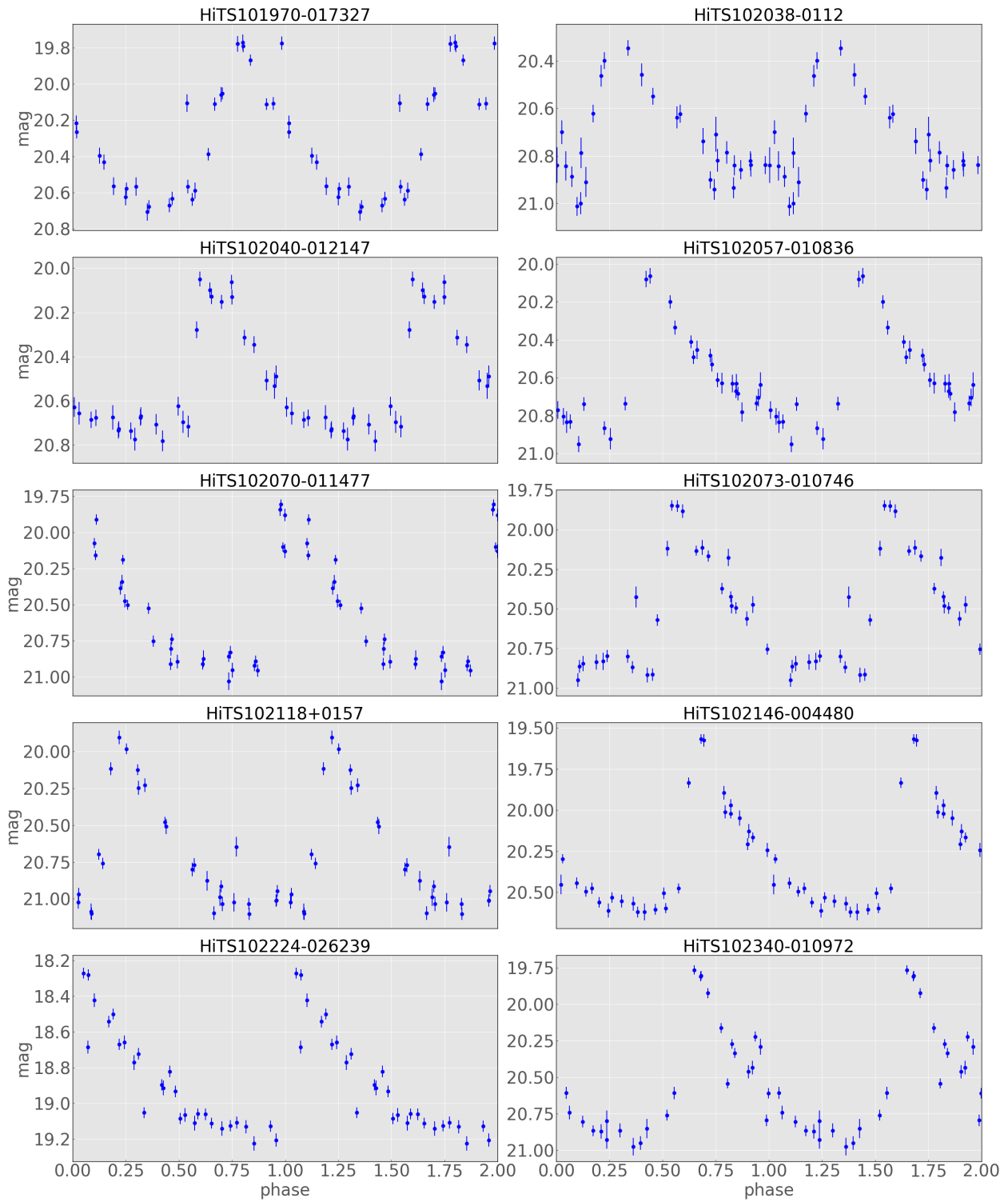


Figure A.3: Phased light curves of RR Lyrae found from HiTS 2015a (3/11)

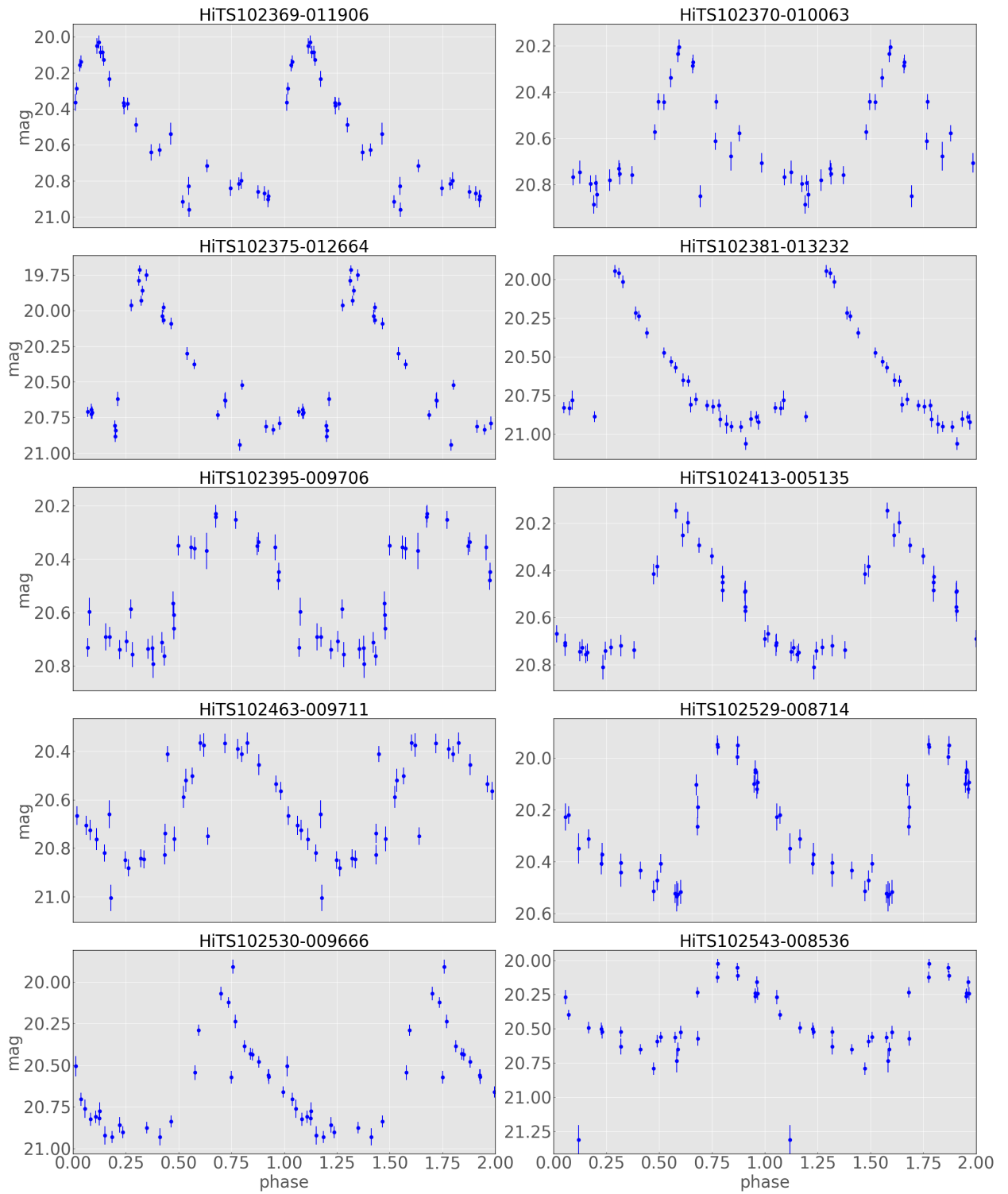


Figure A.4: Phased light curves of RR Lyrae found from HiTS 2015a (4/11)

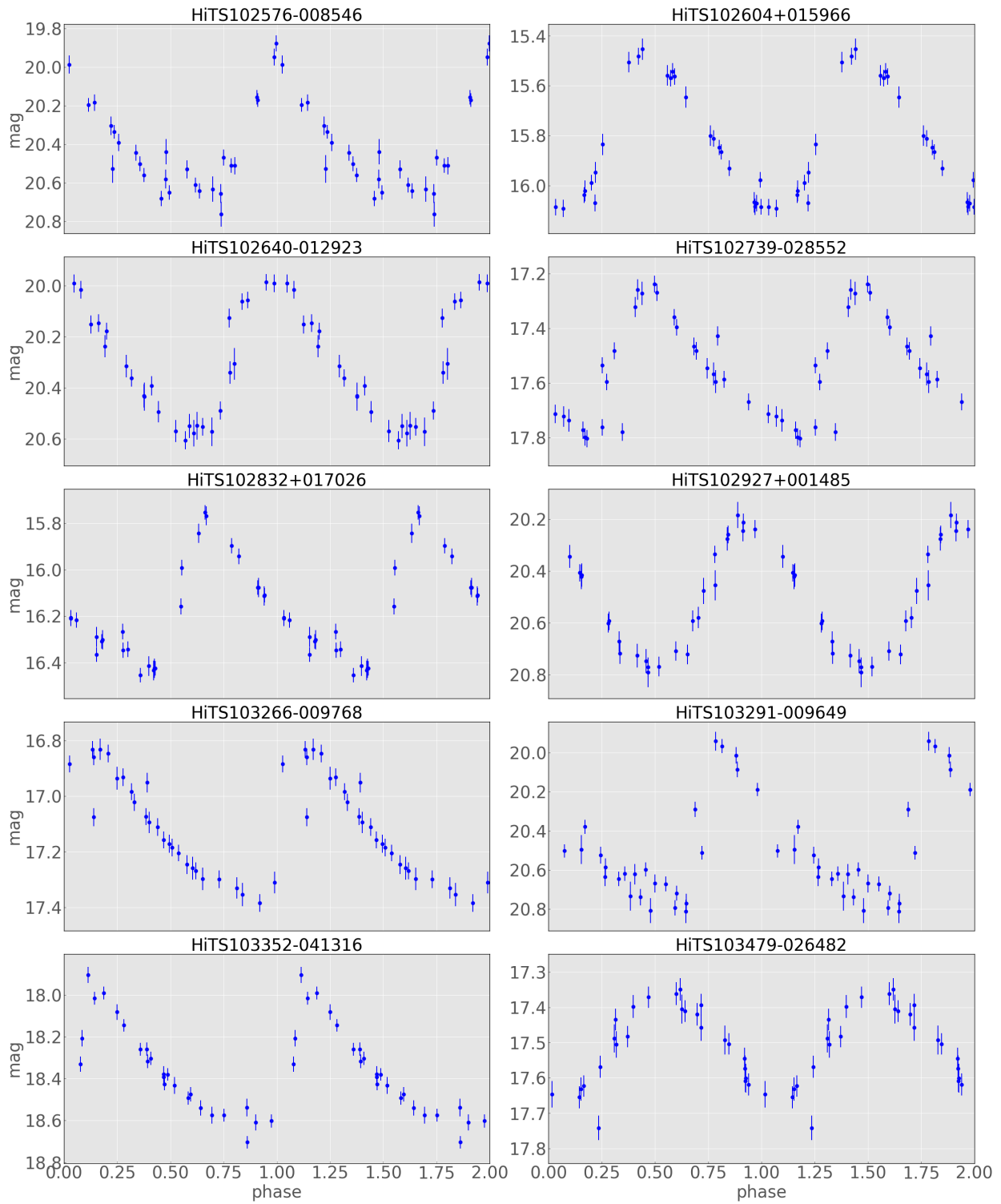


Figure A.5: Phased light curves of RR Lyrae found from HiTS 2015a (5/11)

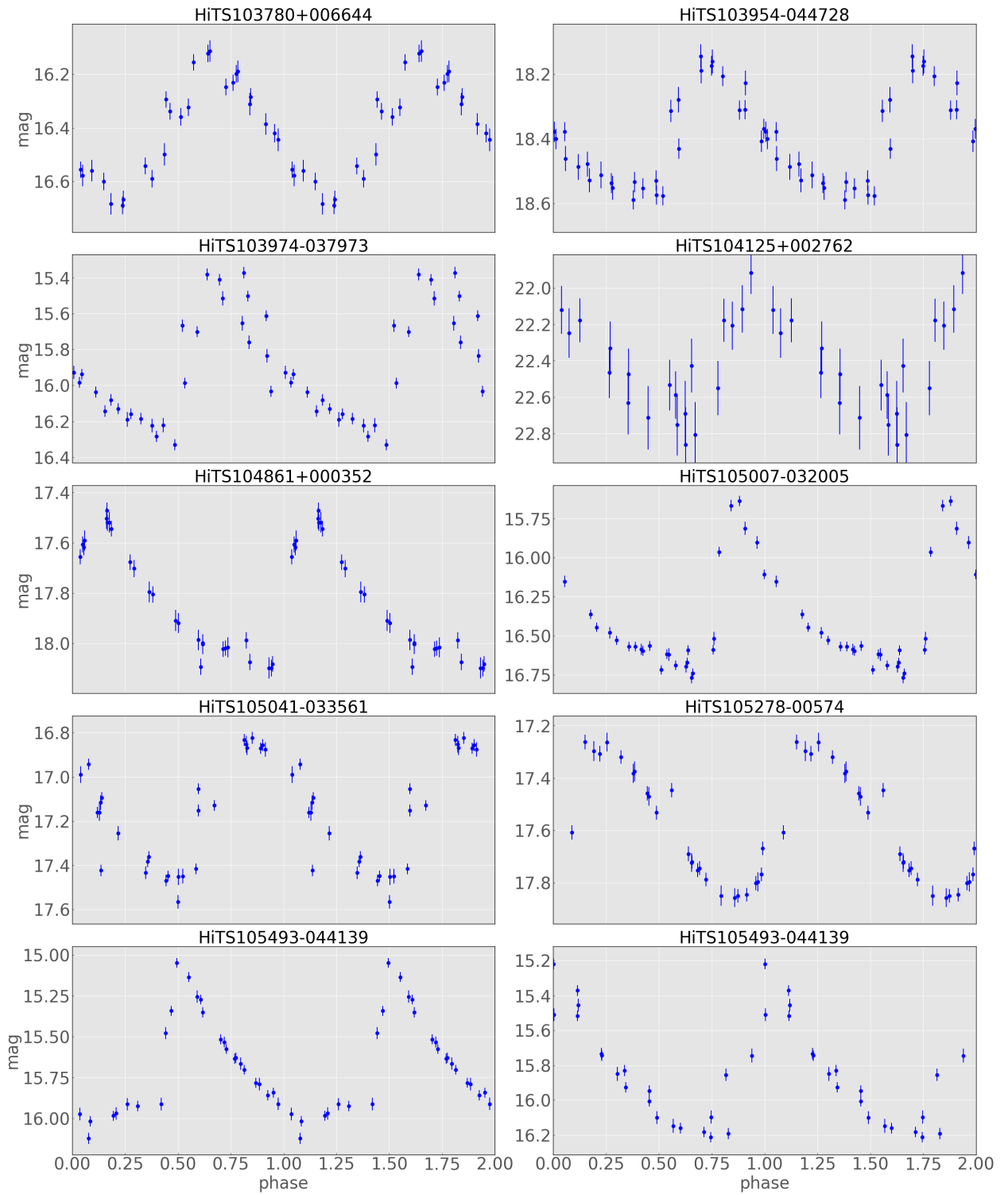


Figure A.6: Phased light curves of RR Lyrae found from HiTS 2015a (6/11)

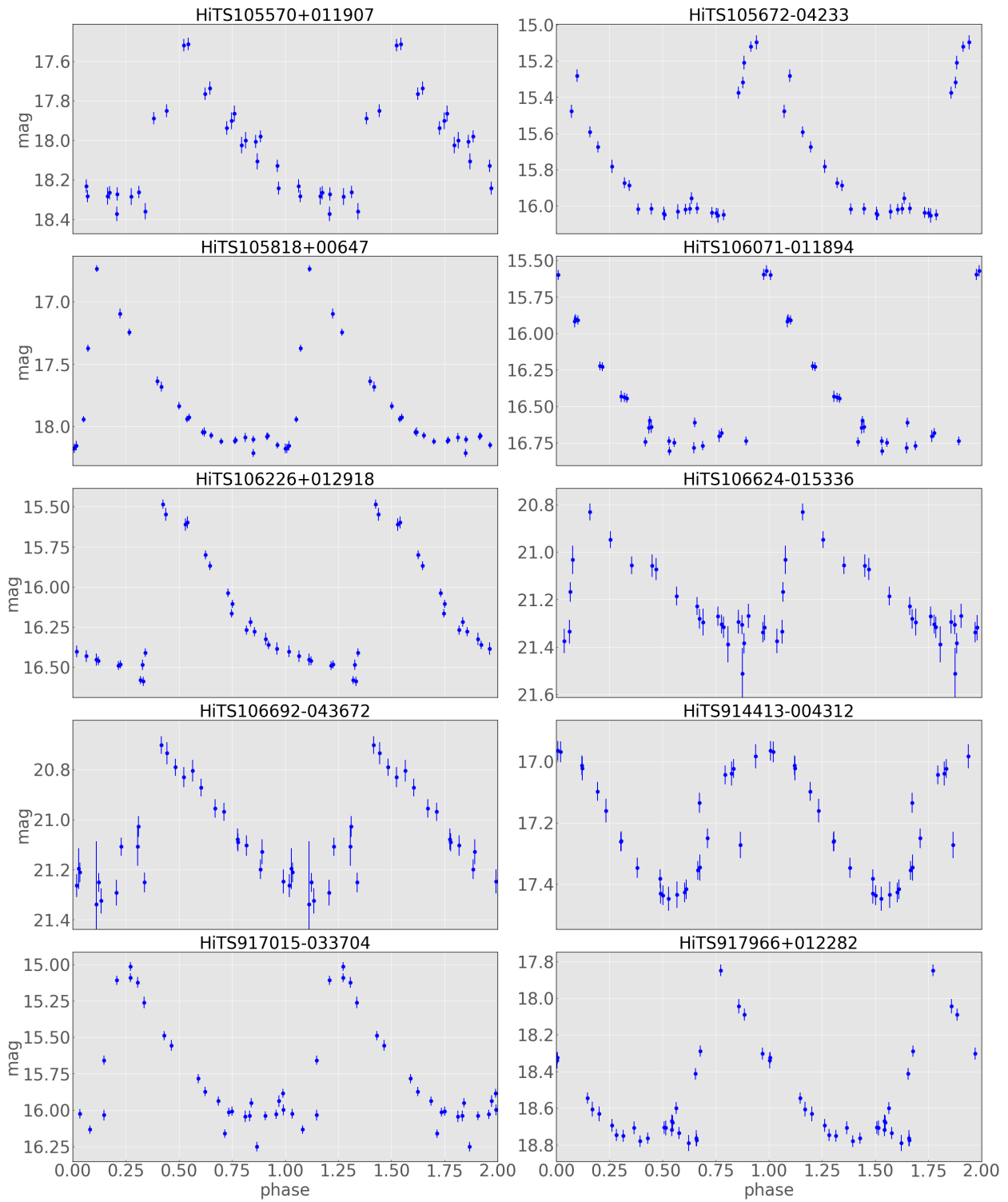


Figure A.7: Phased light curves of RR Lyrae found from HiTS 2015a (7/11)

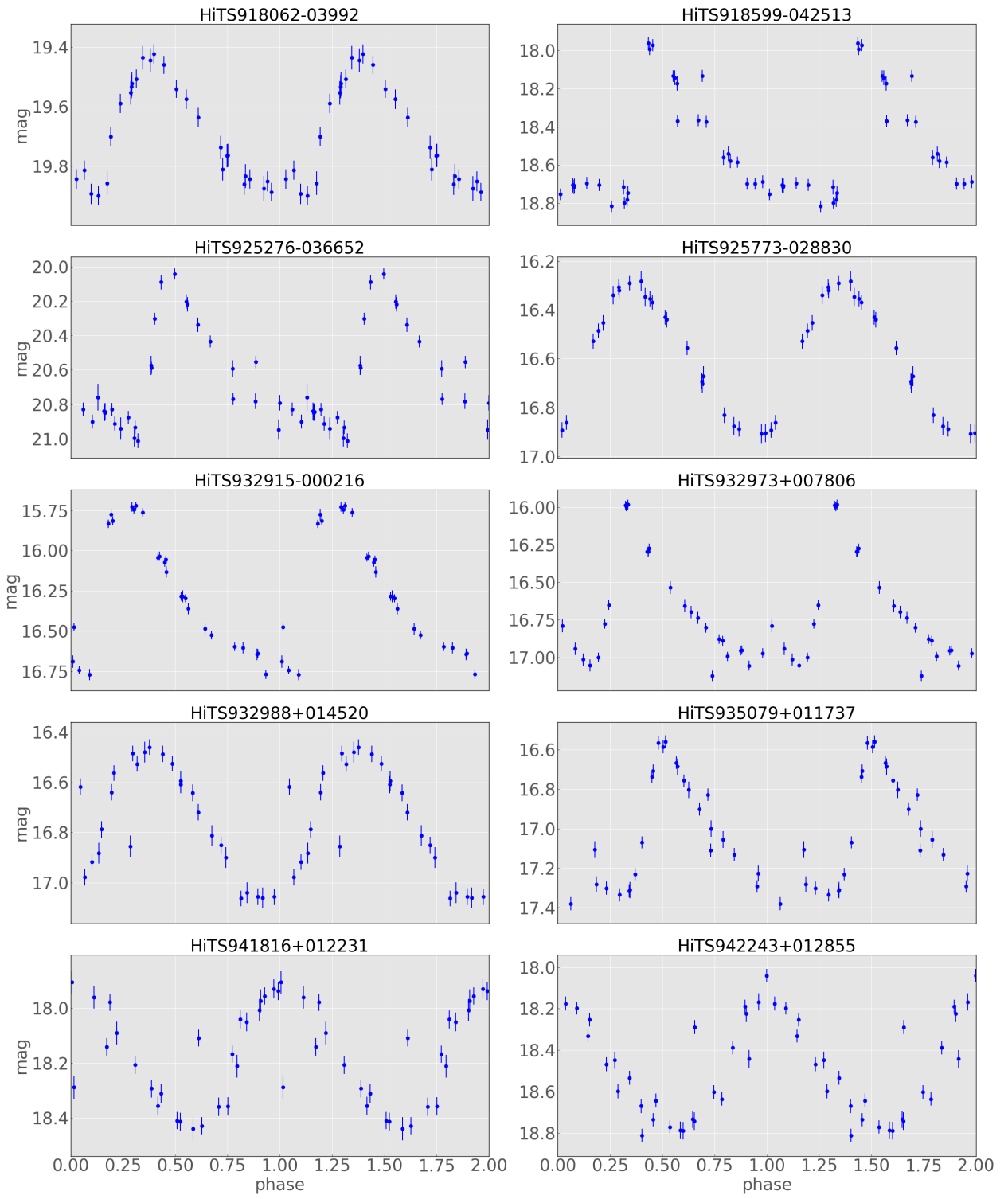


Figure A.8: Phased light curves of RR Lyrae found from HiTS 2015a (8/11)



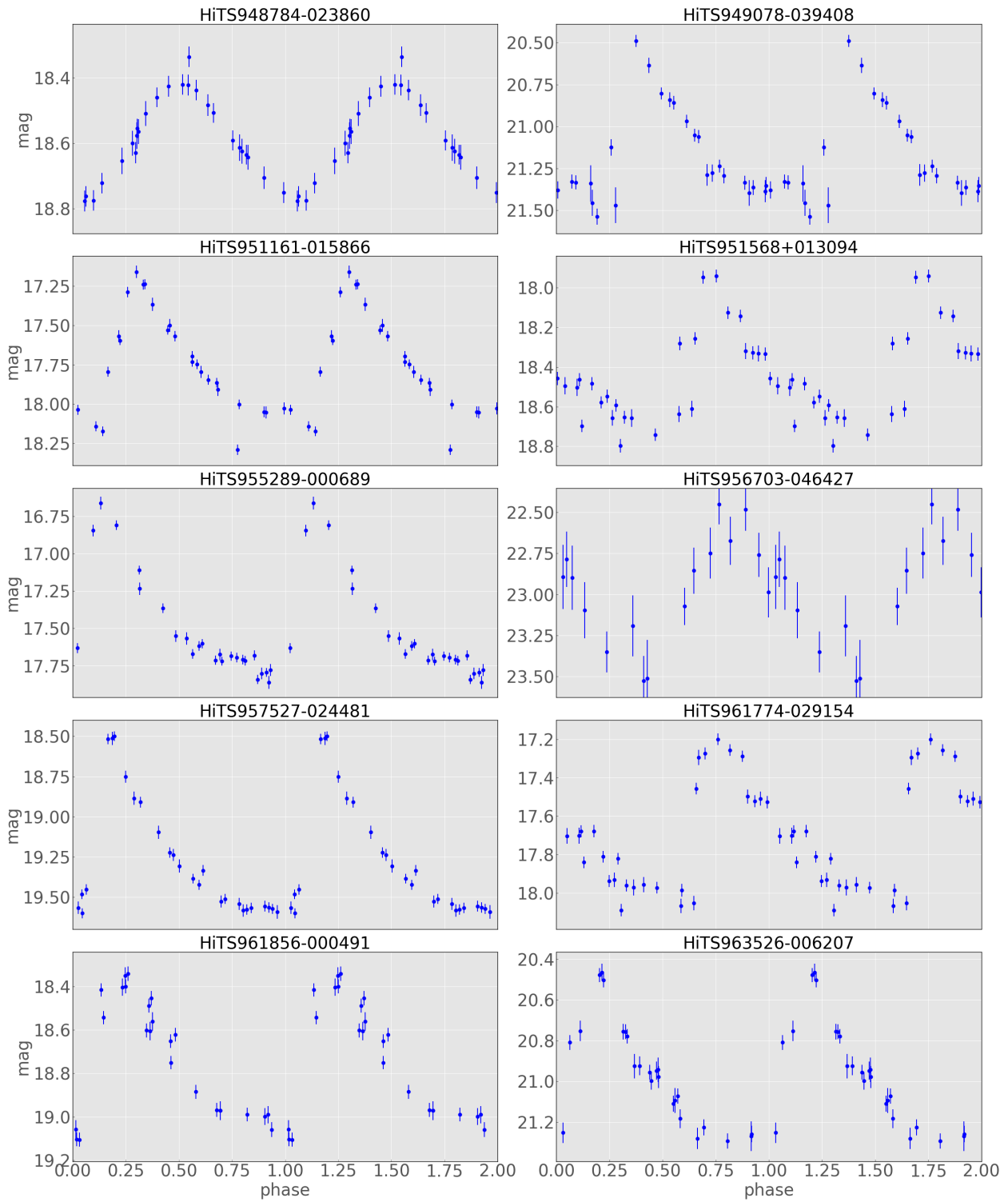


Figure A.9: Phased light curves of RR Lyrae found from HiTS 2015a (9/11)

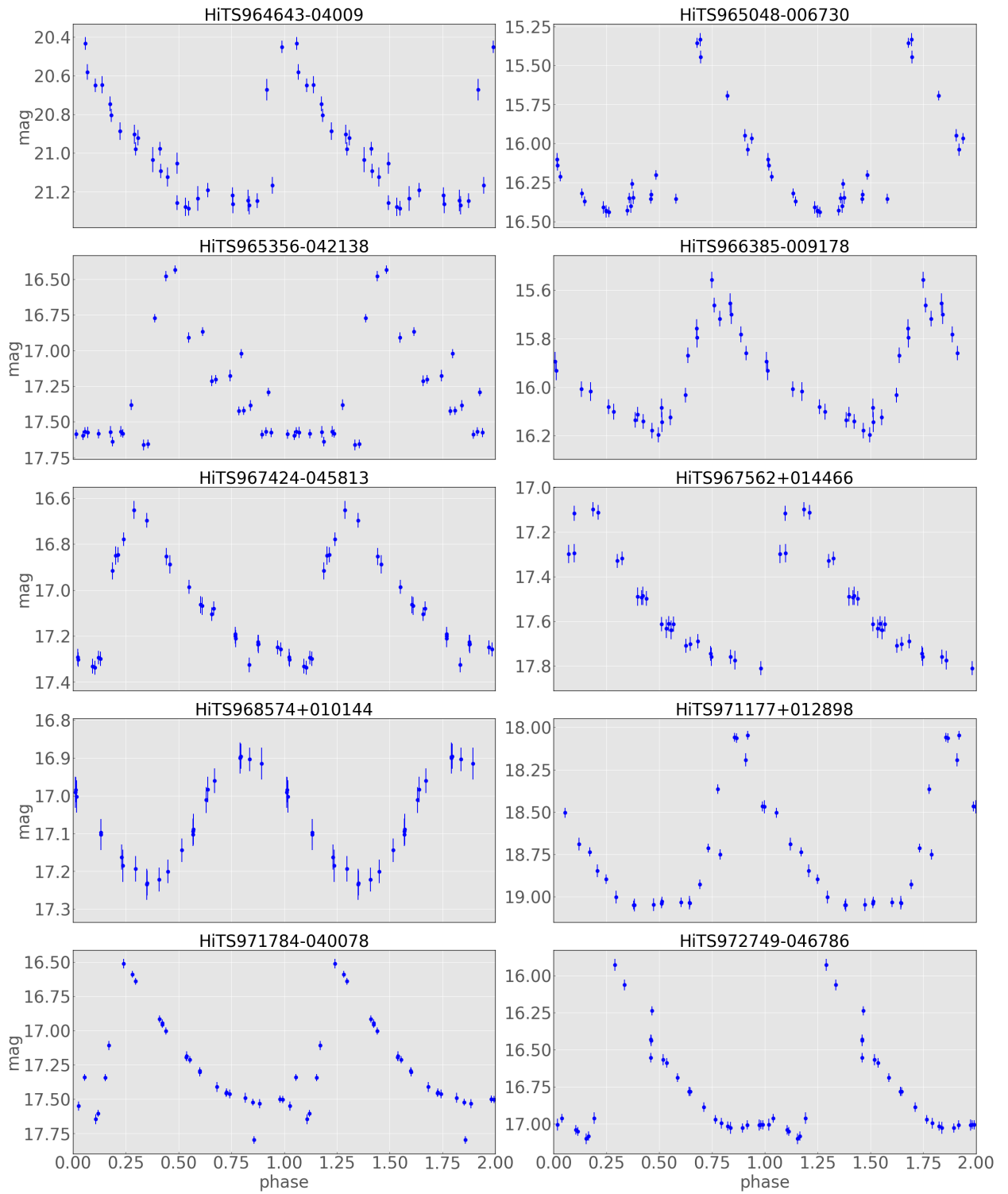


Figure A.10: Phased light curves of RR Lyrae found from HiTS 2015a (10/11)

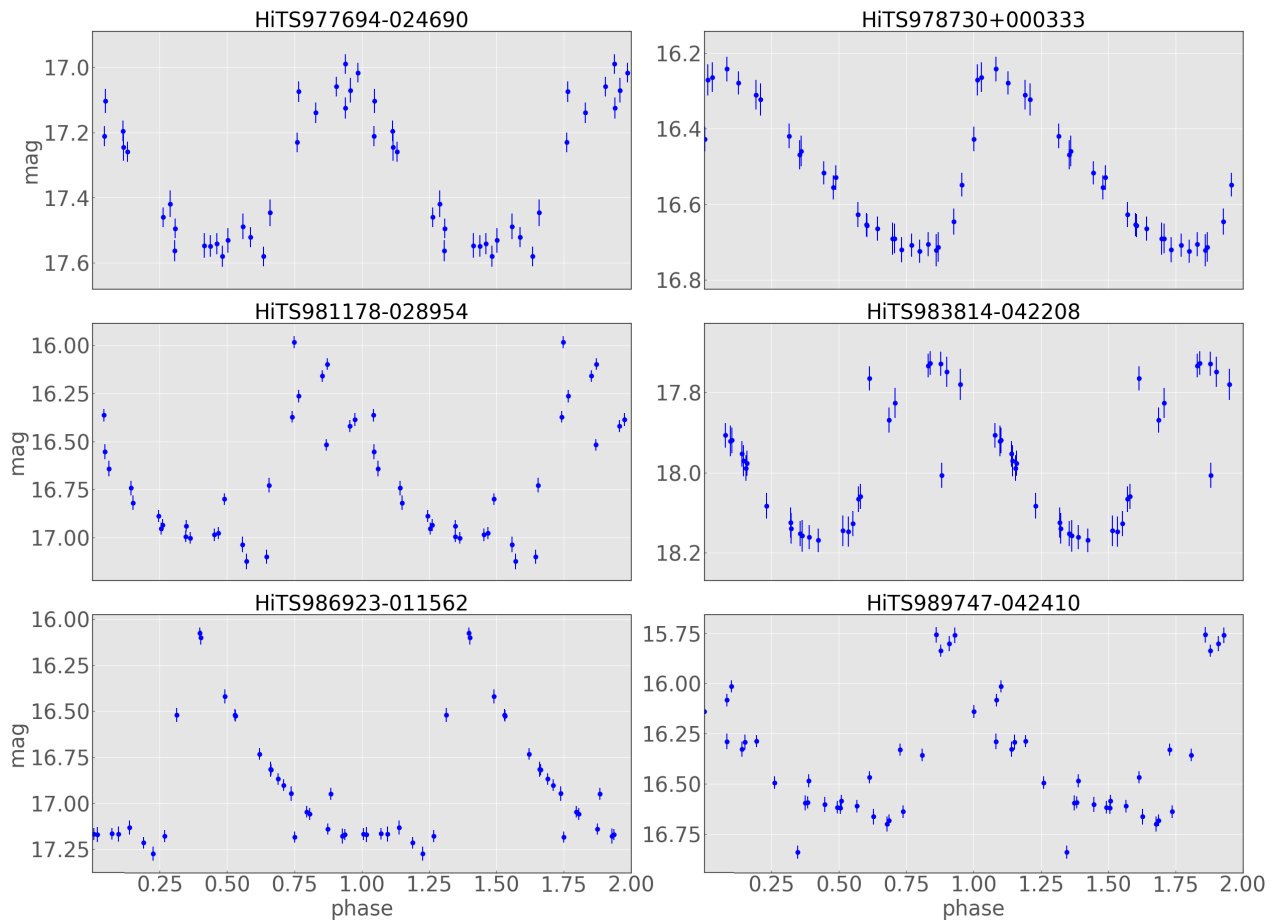


Figure A.11: Phased light curves of RR Lyrae found from HiTS 2015a (11/11)

# Appendix B

## Bibliography

. Instrument - The Dark Energy Survey. <https://www.darkenergysurvey.org/the-des-project/instrument/>. Accessed: 2018-04-27.

. NOAO Science Archive. <http://archive.noao.edu/>. Accessed: 2018-03-26.

. SVA1 GOLD Catalog. <https://opensource.ncsa.illinois.edu/confluence/display/DESDM/SVA1+GOLD+Catalog>. Accessed: 2018-03-21.

. VISTA Data Processing. <http://casu.ast.cam.ac.uk/surveys-projects/vista/data-processing>. Accessed: 2018-03-21.

Ablimit, I. and G. Zhao

2017. The Milky Way's Circular Velocity Curve and Its Constraint on the Galactic Mass with RR Lyrae Stars. *ApJ*, 846:10.

Allevato, V., M. Paolillo, I. Papadakis, and C. Pinto

2013. Measuring X-Ray Variability in Faint/Sparsely Sampled Active Galactic Nuclei. *ApJ*, 771.

Angeloni, R., R. Contreras Ramos, M. Catelan, I. Dékány, F. Gran, J. Alonso-García, M. Hempel, C. Navarrete, H. Andrews, A. Aparicio, J. C. Beamín, C. Berger, J. Borissova, C. Contreras Peña, A. Cunial, R. de Grijs, N. Espinoza, S. Eyheramendy, C. E. Ferreira Lopes, M. Fiaschi, G. Hajdu, J. Han, K. G. Hełminiak, A. Hempel, S. L. Hidalgo, Y. Ita, Y.-B. Jeon, A. Jordán, J. Kwon, J. T. Lee, E. L. Martín, N. Masetti, N. Matsunaga, A. P. Milone, D. Minniti, L. Morelli, F. Murgas, T. Nagayama, C. Navarro, P. Ochner, P. Pérez, K. Pichara, A. Rojas-Arriagada, J. Roquette, R. K. Saito, A. Siviero, J. Sohn, H.-I. Sung, M. Tamura, R. Tata, L. Tomasella, B. Townsend, and P. Whitelock

2014. The VVV Templates Project Towards an automated classification of VVV light-curves. I. Building a database of stellar variability in the near-infrared. *A&A*, 567:A100.

- Bailey, S. I.  
1902. A discussion of variable stars in the cluster  $\omega$  Centauri. *Annals of Harvard College Observatory*, 38:1.
- Benedict, G. F., B. E. McArthur, M. W. Feast, T. G. Barnes, T. E. Harrison, J. L. Bean, J. W. Menzies, B. Chaboyer, L. Fossati, N. Nesvacil, H. A. Smith, K. Kolenberg, C. D. Laney, O. Kochukhov, E. P. Nelan, D. V. Shulyak, D. Taylor, and W. L. Freedman  
2011. Distance Scale Zero Points from Galactic RR Lyrae Star Parallaxes. *AJ*, 142:187.
- Bertin, E. and S. Arnouts  
1996. SExtractor: Software for source extraction. *A&AS*, 117:393–404.
- Blažko, S.  
1907. Mitteilung über veränderliche Sterne. *Astronomische Nachrichten*, 175:327.
- Carroll, B. and D. Ostlie  
2017. *An Introduction to Modern Astrophysics*. Cambridge University Press.
- Cartier, R., P. Lira, P. Coppi, P. Sánchez, P. Arévalo, F. E. Bauer, D. Rabinowitz, R. Zinn, R. R. Muñoz, and N. Meza  
2015. The QUEST-La Silla AGN Variability Survey. *ApJ*, 810:164.
- Catelan, M., B. J. Pritzl, and H. A. Smith  
2004. The RR Lyrae Period-Luminosity Relation. I. Theoretical Calibration. *The Astrophysical Journal Supplement Series*, 154:633–649.
- Catelan, M. and H. Smith  
2014. *Pulsating Stars*. Wiley.
- Clement, C. M., A. Muzzin, Q. Dufton, T. Ponnampalam, J. Wang, J. Burford, A. Richardson, T. Rosebery, J. Rowe, and H. S. Hogg  
2001. Variable Stars in Galactic Globular Clusters. *AJ*, 122:2587–2599.
- Dall’Ora, M., J. Storm, G. Bono, V. Ripepi, M. Monelli, V. Testa, G. Andreuzzi, R. Buonanno, F. Caputo, V. Castellani, C. E. Corsi, G. Marconi, M. Marconi, L. Pulone, and P. B. Stetson  
2004. The Distance to the Large Magellanic Cloud Cluster Reticulum from the K-Band Period-Luminosity-Metallicity Relation of RR Lyrae Stars. *ApJ*, 610:269–274.
- Dalton, G. B., M. Caldwell, A. K. Ward, M. S. Whalley, G. Woodhouse, R. L. Edeson, P. Clark, S. M. Beard, A. M. Gallie, S. P. Todd, J. M. D. Strachan, N. N. Bezawada, W. J. Sutherland, and J. P. Emerson  
2006. The VISTA infrared camera. In *Society of Photo-Optical Instrumentation Engineers (SPIE) Conference Series*, volume 6269 of *Proc. SPIE*, P. 62690X.
- De Lee, N.  
2008. *Exploring the Milky Way halo with SDSS-II SN survey RR Lyrae stars*. PhD thesis, Michigan State University.

- Deb, S. and H. P. Singh  
2009. Light curve analysis of variable stars using Fourier decomposition and principal component analysis. *A&A*, 507:1729–1737.
- Desai, S., R. Armstrong, J. J. Mohr, D. R. Semler, J. Liu, E. Bertin, S. S. Allam, W. A. Barkhouse, G. Bazin, E. J. Buckley-Geer, M. C. Cooper, S. M. Hansen, F. W. High, H. Lin, Y.-T. Lin, C.-C. Ngeow, A. Rest, J. Song, D. Tucker, and A. Zenteno  
2012. The Blanco Cosmology Survey: Data Acquisition, Processing, Calibration, Quality Diagnostics, and Data Release. *ApJ*, 757:83.
- Downes, R. A., B. Margon, L. Homer, and S. F. Anderson  
2004. Far-Ultraviolet Observations of RR Lyrae Stars in the Core of NGC 1851. *AJ*, 128:2288–2294.
- Drake, A. J., M. Catelan, S. G. Djorgovski, G. Torrealba, M. J. Graham, V. Belokurov, S. E. Koposov, A. Mahabal, J. L. Prieto, C. Donalek, R. Williams, S. Larson, E. Christensen, and E. Beshore  
2013a. Probing the Outer Galactic Halo with RR Lyrae from the Catalina Surveys. *ApJ*, 763:32.
- Drake, A. J., M. Catelan, S. G. Djorgovski, G. Torrealba, M. J. Graham, A. Mahabal, J. L. Prieto, C. Donalek, R. Williams, S. Larson, E. Christensen, and E. Beshore  
2013b. Evidence for a Milky Way Tidal Stream Reaching Beyond 100 kpc. *ApJ*, 765:154.
- Eadie, G. M. and W. E. Harris  
2016. Bayesian Mass Estimates of the Milky Way: The Dark and Light Sides of Parameter Assumptions. *ApJ*, 829:108.
- Förster, F., J. C. Maureira, J. San Martín, M. Hamuy, J. Martínez, P. Huijse, G. Cabrera, L. Galbany, T. de Jaeger, S. González-Gaitán, J. P. Anderson, H. Kunkarayakti, G. Pignata, F. Bufano, J. Littín, F. Olivares, G. Medina, R. C. Smith, A. K. Vivas, P. A. Estévez, R. Muñoz, and E. Vera  
2016. The High Cadence Transient Survey (HITS). I. Survey Design and Supernova Shock Breakout Constraints. *ApJ*, 832.
- Gawiser, E., P. G. van Dokkum, D. Herrera, J. Maza, F. J. Castander, L. Infante, P. Lira, R. Quadri, R. Toner, E. Treister, C. M. Urry, M. Altmann, R. Assef, D. Christlein, P. S. Coppi, M. F. Durán, M. Franx, G. Galaz, L. Huerta, C. Liu, S. López, R. Méndez, D. C. Moore, M. Rubio, M. T. Ruiz, S. Toft, and S. K. Yi  
2006. The Multiwavelength Survey by Yale-Chile (MUSYC): Survey Design and Deep Public UBVRIZ Images and Catalogs of the Extended Hubble Deep Field-South. *The Astrophysical Journal Supplement Series*, 162:1–19.
- Ivezic, Z., T. Axelrod, W. N. Brandt, D. L. Burke, C. F. Claver, A. Connolly, K. H. Cook, P. Gee, D. K. Gilmore, S. H. Jacoby, R. L. Jones, S. M. Kahn, J. P. Kantor, V. V. Krabbendam, R. H. Lupton, D. G. Monet, P. A. Pinto, A. Saha, T. L. Schalk, D. P. Schneider, M. A. Strauss, C. W. Stubbs, D. Sweeney, A. Szalay, J. J. Thaler, J. A. Tyson,

and LSST Collaboration

2008. Large Synoptic Survey Telescope: From Science Drivers To Reference Design. *Serbian Astronomical Journal*, 176:1–13.

Jarvis, M., E. Sheldon, J. Zuntz, T. Kacprzak, S. L. Bridle, A. Amara, R. Armstrong, M. R. Becker, G. M. Bernstein, C. Bonnett, C. Chang, R. Das, J. P. Dietrich, A. Drlica-Wagner, T. F. Eifler, C. Gangkofner, D. Gruen, M. Hirsch, E. M. Huff, B. Jain, S. Kent, D. Kirk, N. MacCrann, P. Melchior, A. A. Plazas, A. Refregier, B. Rowe, E. S. Rykoff, S. Samuroff, C. Sánchez, E. Suchyta, M. A. Troxel, V. Vikram, T. Abbott, F. B. Abdalla, S. Allam, J. Annis, A. Benoit-Lévy, E. Bertin, D. Brooks, E. Buckley-Geer, D. L. Burke, D. Capozzi, A. Carnero Rosell, M. Carrasco Kind, J. Carretero, F. J. Castander, J. Clampitt, M. Crocce, C. E. Cunha, C. B. D’Andrea, L. N. da Costa, D. L. DePoy, S. Desai, H. T. Diehl, P. Doel, A. Fausti Neto, B. Flaugher, P. Fosalba, J. Frieman, E. Gaztanaga, D. W. Gerdes, R. A. Gruendl, G. Gutierrez, K. Honscheid, D. J. James, K. Kuehn, N. Kuropatkin, O. Lahav, T. S. Li, M. Lima, M. March, P. Martini, R. Miquel, J. J. Mohr, E. Neilsen, B. Nord, R. Ogando, K. Reil, A. K. Romer, A. Roodman, M. Sako, E. Sanchez, V. Scarpine, M. Schubnell, I. Sevilla-Noarbe, R. C. Smith, M. Soares-Santos, F. Sobreira, M. E. C. Swanson, G. Tarle, J. Thaler, D. Thomas, A. R. Walker, and R. H. Wechsler

2016. The DES Science Verification weak lensing shear catalogues. *MNRAS*, 460:2245–2281.

Johnston, K. V., J. S. Bullock, S. Sharma, A. Font, B. E. Robertson, and S. N. Leitner  
2008. Tracing Galaxy Formation with Stellar Halos. II. Relating Substructure in Phase and Abundance Space to Accretion Histories. *ApJ*, 689:936–957.

Jurcsik, J., Á. Sódor, B. Szeidl, Z. Hurta, M. Váradi, K. Posztobányi, K. Vida, G. Hajdu, Z. Kóvári, I. Nagy, L. Molnár, and B. Belucz

2009. The Konkoly Blazhko Survey: is light-curve modulation a common property of RRab stars? *MNRAS*, 400:1006–1018.

Kistler, M. D., W. C. Haxton, and H. Yüksel

2013. Tomography of Massive Stars from Core Collapse to Supernova Shock Breakout. *ApJ*, 778:81.

Lomb, N. R.

1976. Least-Squares Frequency Analysis of Unequally Spaced Data. *Ap&SS*, 39:447–462.

Longmore, A. J., J. A. Fernley, and R. F. Jameson

1986. RR Lyrae stars in globular clusters : better distances from infrared measurements ? *MNRAS*, 220:279–287.

LSST Science Collaboration, P. A. Abell, J. Allison, S. F. Anderson, J. R. Andrew, J. R. P. Angel, L. Armus, D. Arnett, S. J. Asztalos, T. S. Axelrod, S. Bailey, D. R. Ballantyne, J. R. Bankert, W. A. Barkhouse, J. D. Barr, L. F. Barrientos, A. J. Barth, J. G. Bartlett, A. C. Becker, J. Becla, T. C. Beers, J. P. Bernstein, R. Biswas, M. R. Blanton, J. S. Bloom, J. J. Bochanski, P. Boeshaar, K. D. Borne, M. Bradac, W. N. Brandt, C. R. Bridge, M. E. Brown, R. J. Brunner, J. S. Bullock, A. J. Burgasser, J. H. Burge, D. L. Burke,

P. A. Cargile, S. Chandrasekharan, G. Chartas, S. R. Chesley, Y.-H. Chu, D. Cinabro, M. W. Claire, C. F. Claver, D. Clowe, A. J. Connolly, K. H. Cook, J. Cooke, A. Cooray, K. R. Covey, C. S. Culliton, R. de Jong, W. H. de Vries, V. P. Debattista, F. Delgado, I. P. Dell’Antonio, S. Dhital, R. Di Stefano, M. Dickinson, B. Dilday, S. G. Djorgovski, G. Dobler, C. Donalek, G. Dubois-Felsmann, J. Durech, A. Eliasdottir, M. Eracleous, L. Eyer, E. E. Falco, X. Fan, C. D. Fassnacht, H. C. Ferguson, Y. R. Fernandez, B. D. Fields, D. Finkbeiner, E. E. Figuera, D. B. Fox, H. Francke, J. S. Frank, J. Frieman, S. Fromenteau, M. Furqan, G. Galaz, A. Gal-Yam, P. Garnavich, E. Gawiser, J. Geary, P. Gee, R. R. Gibson, K. Gilmore, E. A. Grace, R. F. Green, W. J. Gressler, C. J. Grillmair, S. Habib, J. S. Haggerty, M. Hamuy, A. W. Harris, S. L. Hawley, A. F. Heavens, L. Hebb, T. J. Henry, E. Hileman, E. J. Hilton, K. Hoadley, J. B. Holberg, M. J. Holman, S. B. Howell, L. Infante, Z. Ivezic, S. H. Jacoby, B. Jain, R. Jedicke, M. J. Jee, J. Garrett Jernigan, S. W. Jha, K. V. Johnston, R. L. Jones, M. Juric, M. Kaasalainen, Styliani, Kafka, S. M. Kahn, N. A. Kaib, J. Kalirai, J. Kantor, M. M. Kasliwal, C. R. Keeton, R. Kessler, Z. Knezevic, A. Kowalski, V. L. Krabbendam, K. S. Krughoff, S. Kulkarni, S. Kuhlman, M. Lacy, S. Lepine, M. Liang, A. Lien, P. Lira, K. S. Long, S. Lorenz, J. M. Lotz, R. H. Lupton, J. Lutz, L. M. Macri, A. A. Mahabal, R. Mandelbaum, P. Marshall, M. May, P. M. McGehee, B. T. Meadows, A. Meert, A. Milani, C. J. Miller, M. Miller, D. Mills, D. Minniti, D. Monet, A. S. Mukadam, E. Nakar, D. R. Neill, J. A. Newman, S. Nikolaev, M. Nordby, P. O’Connor, M. Oguri, J. Oliver, S. S. Olivier, J. K. Olsen, K. Olsen, E. W. Olszewski, H. Oluseyi, N. D. Padilla, A. Parker, J. Pepper, J. R. Peterson, C. Petry, P. A. Pinto, J. L. Pizagno, B. Popescu, A. Prsa, V. Radcka, M. J. Raddick, A. Rasmussen, A. Rau, J. Rho, J. E. Rhoads, G. T. Richards, S. T. Ridgway, B. E. Robertson, R. Roskar, A. Saha, A. Sarajedini, E. Scannapieco, T. Schalk, R. Schindler, S. Schmidt, S. Schmidt, D. P. Schneider, G. Schumacher, R. Scranton, J. Sebag, L. G. Seppala, O. Shemmer, J. D. Simon, M. Sivertz, H. A. Smith, J. Allyn Smith, N. Smith, A. H. Spitz, A. Stanford, K. G. Stassun, J. Strader, M. A. Strauss, C. W. Stubbs, D. W. Sweeney, A. Szalay, P. Szkody, M. Takada, P. Thorman, D. E. Trilling, V. Trimble, A. Tyson, R. Van Berg, D. Vanden Berk, J. VanderPlas, L. Verde, B. Vrsnak, L. M. Walkowicz, B. D. Wandelt, S. Wang, Y. Wang, M. Warner, R. H. Wechsler, A. A. West, O. Wiecha, B. F. Williams, B. Willman, D. Wittman, S. C. Wolff, W. M. Wood-Vasey, P. Wozniak, P. Young, A. Zentner, and H. Zhan

2009. LSST Science Book, Version 2.0. *ArXiv e-prints*, P. arXiv:0912.0201.

McCracken, H. J., B. Milvang-Jensen, J. Dunlop, M. Franx, J. P. U. Fynbo, O. Le Fèvre, J. Holt, K. I. Caputi, Y. Goranova, F. Buitrago, J. P. Emerson, W. Freudling, P. Hudelot, C. López-Sanjuan, F. Magnard, Y. Mellier, P. Möller, K. K. Nilsson, W. Sutherland, L. Tasca, and J. Zabl

2012. UltraVISTA: a new ultra-deep near-infrared survey in COSMOS. *A&A*, 544:A156.

McLaughlin, M. A., J. R. Mattox, J. M. Cordes, and D. J. Thompson

1996. Variability of CGRO/EGRET Gamma-Ray Sources. *ApJ*, 473:763.

Medina, G.

2017. Searching for distant rr lyrae in the galactic halo using the high cadence transient survey. Master’s thesis, Universidad de Chile.



- Medina, G. E., R. R. Muñoz, A. K. Vivas, J. L. Carlin, F. Förster, J. Martínez, L. Galbany, S. González-Gaitán, M. Hamuy, T. de Jaeger, J. C. Maureira, and J. San Martín  
2018. Discovery of Distant RR Lyrae Stars in the Milky Way Using DECam. *ApJ*, 855:43.
- Mighell, K. J.  
2010. Crblaster: A parallel-processing computational framework for embarrassingly parallel image-analysis algorithms. *Publications of the Astronomical Society of the Pacific*, 122(896):1236.
- Muraveva, T., H. E. Delgado, G. Clementini, L. M. Sarro, and A. Garofalo  
2018. RR Lyrae stars as standard candles in the Gaia Data Release 2 Era. *ArXiv e-prints*, P. arXiv:1805.08742.
- Muzzin, A., D. Marchesini, M. Stefanon, M. Franx, B. Milvang-Jensen, J. S. Dunlop, J. P. U. Fynbo, G. Brammer, I. Labbé, and P. van Dokkum  
2013. A Public  $K_s$ -selected Catalog in the COSMOS/ULTRAVISTA Field: Photometry, Photometric Redshifts, and Stellar Population Parameters. *The Astrophysical Journal Supplement Series*, 206:8.
- Nandra, K., I. M. George, R. F. Mushotzky, T. J. Turner, and T. Yaqoob  
1997. ASCA Observations of Seyfert 1 Galaxies. I. Data Analysis, Imaging, and Timing. *ApJ*, 476:70–82.
- Oluseyi, H. M., A. C. Becker, C. Culliton, M. Furqan, K. L. Hoadley, P. Regencia, A. J. Wells, Ž. Ivezić, R. L. Jones, K. S. Krughoff, B. Sesar, S. Jacoby, and I. J. Allison  
2012. Simulated LSST Survey of RR Lyrae Stars throughout the Local Group. *AJ*, 144:9.
- Pickering, E. C., H. R. Colson, W. P. Fleming, and L. D. Wells  
1901. Sixty-four new variable stars. *ApJ*, 13.
- Samus, N. N., E. V. Kazarovets, O. V. Durlevich, N. N. Kireeva, and E. N. Pastukhova  
2017. General catalogue of variable stars: Version GCVS 5.1. *Astronomy Reports*, 61:80–88.
- Sánchez, P., P. Lira, R. Cartier, V. Pérez, N. Miranda, C. Yovanin, P. Arévalo, B. Milvang-Jensen, J. Fynbo, J. Dunlop, P. Coppi, and S. Marchesi  
2017. Near-infrared Variability of Obscured and Unobscured X-Ray-selected AGNs in the COSMOS Field. *ApJ*, 849:110.
- Scovaccicchi, D., R. C. Nichol, D. Bacon, M. Sullivan, and S. Prajs  
2016. Cosmology with superluminous supernovae. *MNRAS*, 456:1700–1707.
- Sesar, B., C. J. Grillmair, J. G. Cohen, E. C. Bellm, V. B. Bhargava, D. Levitan, R. R. Laher, E. O. Ofek, J. A. Surace, S. Tang, A. Waszczak, S. R. Kulkarni, and T. A. Prince  
2013. Tracing the Orphan Stream to 55 kpc with RR Lyrae Stars. *ApJ*, 776:26.
- Sesar, B., N. Hernitschek, S. Mitrović, Ž. Ivezić, H.-W. Rix, J. G. Cohen, E. J. Bernard, E. K. Grebel, N. F. Martin, E. F. Schlafly, W. S. Burgett, P. W. Draper, H. Flewelling, N. Kaiser, R. P. Kudritzki, E. A. Magnier, N. Metcalfe, J. L. Tonry, and C. Waters  
2017. Machine-learned Identification of RR Lyrae Stars from Sparse, Multi-band Data:

- The PS1 Sample. *AJ*, 153:204.
- Shapley, H.  
1916. On the changes in the spectrum, period, and lightcurve of the Cepheid variable RR Lyrae. *ApJ*, 43:217–233.
- Simon, J. D., M. Geha, Q. E. Minor, G. D. Martinez, E. N. Kirby, J. S. Bullock, M. Kaplinghat, L. E. Strigari, B. Willman, P. I. Choi, E. J. Tollerud, and J. Wolf  
2011. A Complete Spectroscopic Survey of the Milky Way Satellite Segue 1: The Darkest Galaxy. *ApJ*, 733:46.
- Skillen, I., R. F. Jameson, J. A. Fernley, A. E. Lynas-Gray, and A. J. Longmore  
1989. The absolute magnitudes of RR Lyrae stars. II - DX Delphini. *MNRAS*, 241:281–294.
- Smith, H.  
2004. *RR Lyrae Stars*, Cambridge Astrophysics. Cambridge University Press.
- Smith, H. A., M. Catelan, and C. Kuehn  
2011. RR Lyrae Period-Amplitude Diagrams: From Bailey to Today. In *RR Lyrae Stars, Metal-Poor Stars, and the Galaxy*, A. McWilliam, ed., volume 5, P. 17.
- Sutherland, W., J. Emerson, G. Dalton, E. Atad-Ettinger, S. Beard, R. Bennett, N. Beza-wada, A. Born, M. Caldwell, P. Clark, S. Craig, D. Henry, P. Jeffers, B. Little, A. McPherson, J. Murray, M. Stewart, B. Stobie, D. Terrett, K. Ward, M. Whalley, and G. Woodhouse  
2015. The Visible and Infrared Survey Telescope for Astronomy (VISTA): Design, technical overview, and performance. *A&A*, 575:A25.
- The Dark Energy Survey Collaboration  
2005. The Dark Energy Survey. *ArXiv Astrophysics e-prints*.
- Valdes, F., R. Gruendl, and DES Project  
2014. The DECam Community Pipeline. In *Astronomical Data Analysis Software and Systems XXIII. Proceedings of a meeting held 29 September - 3 October 2013 at Waikoloa Beach Marriott, Hawaii, USA. Edited by N. Manset and P. Forshay ASP conference series, vol. 485, 2014, p.379*, volume 485, P. 379.
- Vanderplas, J., A. Connolly, Ž. Ivezić, and A. Gray  
2012. Introduction to astroml: Machine learning for astrophysics. In *Conference on Intelligent Data Understanding (CIDU)*, Pp. 47–54.
- VanderPlas, J. T.  
2017. Understanding the Lomb-Scargle Periodogram. *ArXiv e-prints*.
- Vivas, A. K., K. Olsen, R. Blum, D. L. Nidever, A. R. Walker, N. F. Martin, G. Besla, C. Gallart, R. P. van der Marel, S. R. Majewski, C. C. Kaleida, R. R. Muñoz, A. Saha, B. C. Conn, and S. Jin  
2016. Variable Stars in the Field of the Hydra II Ultra-faint Dwarf Galaxy. *AJ*, 151:118.
- Zechmeister, M. and M. Kürster

2009. The generalised Lomb-Scargle periodogram. A new formalism for the floating-mean and Keplerian periodograms. *A&A*, 496:577–584.

Zinn, R., B. Horowitz, A. K. Vivas, C. Baltay, N. Ellman, E. Hadjiyska, D. Rabinowitz, and L. Miller

2014. La Silla QUEST RR Lyrae Star Survey: Region I. *ApJ*, 781:22.